# Identification of region-specific astrocyte subtypes at single cell resolution

# Identification of region-specific astrocyte subtypes at single cell resolution

Mykhailo Y. Batiuk[1,2§†], Araks Martirosyan[1,2§], Jérôme Wahis[1,2], Filip de Vin[1,2], Catherine Marneffe[1,2], Carola Kusserow[1,2], Jordan Koeppen[1,2], João Filipe Viana[3,4], João Filipe Oliveira[3,4,5], Thierry Voet[6,7], Chris P. Ponting[6,8,9], T. Grant Belgard[8‡], Matthew G. Holt[1,2,10*]

[1]Laboratory of Glia Biology, VIB-KU Leuven Center for Brain and Disease Research, Leuven, Belgium
[2]Laboratory of Glia Biology, KU Leuven Department of Neuroscience, Leuven, Belgium
[3]Life and Health Sciences Research Institute (ICVS), University of Minho, Braga, Portugal
[4]ICVS/3Bs - PT Government Associate Laboratory, Braga, Portugal
[5]IPCA-EST-2Ai, Polytechnic Institute of Cávado and Ave, Applied Artificial Intelligence Laboratory, IPCA Campus, Barcelos, Portugal
[6]Sanger Institute–EBI Single-Cell Genomics Centre, Wellcome Trust Sanger Institute, Hinxton, UK
[7]KU Leuven Department of Human Genetics, Leuven, Belgium
[8]MRC Functional Genomics Unit, Department of Physiology, Anatomy & Genetics, University of Oxford, Oxford, UK
[9]MRC Human Genetics Unit, Institute of Genetics and Molecular Medicine, University of Edinburgh, Edinburgh, UK.
[10]Leuven Brain Institute, KU Leuven, Belgium

[§]These authors contributed equally to this work
*To whom correspondence should be addressed:
Dr. Matthew Holt
Herestraat 49, B-3000 Leuven
Belgium
Email: Matthew.Holt@kuleuven.vib.be
Tel: +32 16 37 31 27
Fax: +32 16 37 27 00

[†]Present address: Biotech Research and Innovation Centre, University of Copenhagen, Copenhagen, Denmark.
‡Present address: The Bioinformatics CRO, Niceville, FL 32578, USA

**Astrocytes, a major cell type found throughout the central nervous system, have general roles in the modulation of synapse formation and synaptic transmission, blood-brain-barrier formation and regulation of blood flow, as well as metabolic support of other brain resident cells. Crucially, emerging evidence shows specific adaptations and astrocyte-encoded functions in regions such as spinal cord and cerebellum. To investigate the true extent of astrocyte molecular diversity across forebrain regions, we used single cell RNA sequencing. Our analysis identifies five transcriptomically distinct astrocyte subtypes in adult mouse cortex and hippocampus. Validation of our data *in situ* reveals distinct spatial positioning of defined subtypes, reflecting the distribution of morphologically and physiologically distinct astrocyte populations. Our findings are evidence for specialized astrocyte subtypes between and within brain regions. The data are available through an online database (https://holt-sc.glialab.org/), providing a resource on which to base explorations of local astrocyte diversity and function in the brain.**

## INTRODUCTION

Astrocytes are ubiquitous in the central nervous system (CNS). They possess thousands of individual processes which extend out into the neuropil, interacting with neurons, other glia and blood vessels. Paralleling the wide diversity of their interactions, astrocytes have been reported to play key roles in supporting CNS structure, metabolism, blood-brain-barrier formation and control of vascular blood flow, axon guidance, synapse formation and modulation of synaptic transmission[1].

This degree of functional diversity begs the question of whether astrocytes are a homogeneous group of cells or exist in distinct subtypes with specialized functions. Extensive morphological heterogeneity of astrocyte populations was described over 100 years ago in seminal work by Cajal[2]. Since then, our understanding of the molecular and cellular heterogeneity of astrocytes has remained largely unaltered: astrocyte classification has largely been restricted to two morphological groupings, fibrous and protoplasmic astrocytes, found in the white and grey matter of the brain, respectively. The question of whether specialized astrocyte subtypes exist remains poorly resolved, largely due to the lack of experimental tools allowing detailed astrocyte characterization[3]. This is in contrast to studies on neurons, for which numerous experimental tools exist and evidence for substantial diversity within brain regions has accumulated[4, 5].

However, the issue of astrocyte diversity is now being addressed and a number of studies are reporting heterogeneity of form and function, both between and within brain regions (see reviews by Khakh and Sofroniew[6], Ben Haim and Rowitch[7], Khakh and Deneen[3] and

references therein). The expression of fluorescent reporter tags in astrocytes has allowed the isolation of cells from specific brain regions for RNA[8, 9] profiling and proteomic studies[10]. Fusion of reporter tags to ribosomal subunits (TRAP technology) has permitted the isolation of actively translated mRNAs from astrocytes[10, 11, 12]. Together, these studies revealed that gene expression varies between brain regions and that there is often a subtle gradient of gene expression within individual brain areas. In addition, astrocytes in different brain regions also have distinct morphological and functional features, such as degree of synapse association[9, 10], intrinsic membrane properties and $Ca^{2+}$ signaling[10], and ability to promote neuronal maturation[12]. Refined labeling strategies using promoter fragments[13], or intersectional approaches[14, 15] to isolate subpopulations of cells have revealed intra-regional heterogeneity in cortex[13, 14, 15], as well as brainstem, thalamus, olfactory bulb, cerebellum and spinal cord[14], which again correlates to morphology[15], cell intrinsic physiology[15] and function[13, 14].

Astrocytes are also involved in disease, as evidenced by extensive cell culture and mouse model studies[6], with disruption of astrocyte functions, such as synapse formation, leading to neuronal network dysfunction[13, 14]. Astrocyte heterogeneity may underpin the differential transcriptomic responses seen to bacterial infection (LPS treatment) and stroke (middle cerebral artery occlusion)[16] in mouse astrocytes, as well as in response to demyelination in the EAE model[17], suggesting that successful treatment may have to take account of cell type and brain region, insult and insult severity. One possible reason for the regional difference in tumor susceptibility in the CNS is the location-dependent ability of astrocytes to proliferate, due to differential expression of tumor suppressor genes[18]. Given that analysis of gene co-variation patterns from human tissue samples indicates regional specific astrocyte subtypes[19], it is possible that heterogeneity plays a role in human conditions, such as Norrie disease[13].

Single cell analysis approaches are revolutionizing our concepts of cell identity and heterogeneity. Widely used in the CNS, they have revealed a high diversity of neuronal subtypes across brain regions[4, 5]. In comparison, astrocyte diversity is reported to be low. Whether this reflects the true nature of astrocytes, or is due to technical issues such as low RNA content[20], remains an open question. Consequently, to address the diversity of astrocyte types in the adult mouse brain, we systematically optimized the Smart-seq2 protocol[21], including changes to cell isolation steps and library preparation. We used this pipeline to obtain full-length coverage of cDNAs prepared from thousands of individual astrocytes from adult mouse cortex and hippocampus, areas selected for their well-studied anatomy, physiology, and broad disease relevance. Cluster-based analysis revealed 5 molecularly distinct astrocyte subtypes, which were confirmed *in situ* in the mouse brain. By mapping the spatial position of each subtype, we found a more refined organization of CNS tissue than previously anticipated, with unique molecular astrocyte subtypes occupying distinct

positions, suggestive of specific intra-regional functions. Furthermore, this spatial patterning correlated to the positions of astrocytes with unique morphologies and $Ca^{2+}$ signaling. Our data provide a valuable resource for future hypothesis-driven experiments, aimed at dissecting out the contributions of astrocyte subtypes to CNS function – and are freely available in a standalone database accessible at https://holt-sc.glialab.org/. Such insights might be important to our future understanding of regional susceptibility to diseases, such as Alzheimer's and Parkinson's, in which astrocytes are increasingly implicated[22].

## RESULTS

### Single cell mRNA sequencing reveals astrocyte heterogeneity

To obtain an unbiased and comprehensive comparison of astrocytes in mouse cortex and hippocampus, we performed single cell RNA sequencing. Although dissociating adult mammalian brain tissue into healthy and representative cell suspensions is challenging, astrocytes show transcriptional changes during development (such as in glutamatergic signaling)[23], which can obscure gene-expression differences underlying the functional specialization of cell types[5]. To avoid these issues, we recovered cortex and hippocampus from C57Bl/6J mice aged to post-natal (P) day 56, which should avoid introducing bias from transcriptional programs associated with development[5], while maintaining compatibility with external gene expression databases, such as the Allen Brain Atlas[24]. A single cell suspension for each brain region was obtained using a papain-based protocol, which was previously shown to give good tissue dissociation, with high levels of cell viability[25]. As adult brain is heavily myelinated, a Percoll gradient was used to reduce contamination, while ensuring efficient cell recovery (Supplementary Figure 1, Supplementary Note 1). Astrocytes were then labeled with the ACSA-2 antibody (conjugated to the fluorophore phycoerythrin: PE). This antibody specifically recognizes the plasma membrane marker ATP1B2, which is detected at both the mRNA[20] and protein[25] levels in astrocytes through the adult mouse cortex and hippocampus (Supplementary Figure 2). As mature oligodendrocytes express low levels of ATP1B2, staining with an anti-O1 antibody conjugated to eFluor660 was also performed (Supplementary Figure 3). Viable astrocytes (as determined with 7-AAD staining) were isolated by FACS, with one cell deposited per single well of a PCR plate (Supplementary Figure 4). Preparation of sequencing libraries was done using the Smart-seq2 protocol[21], in which the concentration of template switching oligonucleotide (TSO), number of PCR preamplification cycles and the DNA clean-up step were optimized for use with cells with low RNA content[21] (Figure 1a). (Methods, Supplementary Figures 5-6, Supplementary Note 1). 2,976 individual libraries were sequenced to optimal coverage (~1 million reads per cell) (Figure 1b). Low quality libraries were removed based on FastQC and additional quality metrics (see Methods and Supplementary Figure 7), leaving 2,015 high quality libraries. On

average, each of these contained 83% exonic reads, mapping to 2,148 genes, with only 11% intronic and 6% intergenic reads (Figure 1b).

Clustering analysis was performed using Seurat[26]. Analysis of these libraries revealed a residual fraction of contaminating higher order CNS cell types (Figure 1c, d, Supplementary Table 1). Cell type identification was based on the expression of known marker genes (Figure 1c). Following removal of contaminating cell types, 1,811 astrocytes remained. These cells were then re-clustered, based on the 886 highly variable genes expressed across astrocytes (see Methods for more details). This led to the identification of 5 distinct Astrocyte SubTypes (AST1-5), each distinguished by a gene expression fingerprint (Figure 2a, b). tSNE plots showed three major 'clouds' of cells. AST4 and AST5 formed distinct clusters, suggesting distinct molecular fingerprints. In contrast, ASTs 1-3 were grouped together, suggesting much more subtle differences in gene expression between these subtypes (Figure 2a, Supplementary Figure 8). Astrocyte subtypes constituted different proportions of the total cell population analyzed using our optimized Smart-seq2 protocol, ranging from 1.4% (AST5) to 36.5% (AST1) (Supplementary Table 2).

As expected, there was clear separation of subtypes between cortex and hippocampus[11, 12] (Figure 2c, Supplementary Table 2), with AST1 and AST4 being predominantly hippocampal, AST2 being mainly cortical, and AST3 and AST5 being distributed uniformly between brain regions. As control experiments effectively excluded clustering by batch effects during sample processing (Supplementary File 1 and https://holt-sc.glialab.org/sc/), these data confirmed that our protocol could identify both inter- and intra-regional heterogeneity of astrocytes in adult mouse brain.

**Unique molecular signatures define astrocyte subtypes**

Analysis of sequencing data showed a number of genes common across astrocytes (expressed in more than 60% of cells). However, the astrocyte subtypes we identified also showed enrichment of specific genes (Figures 2d, 3a). To gain insight into the possible roles played by differential gene expression, we analyzed transcript lists using gene enrichment and functional annotation (DAVID)-based approaches[27], and manual curation using the UniProt database[28].

Genes commonly expressed across astrocytes (Supplementary File 2) include transcription factors known to play a role in neural patterning (*Dbx2*) and astrocyte specification (*Sox9*). Perhaps unsurprisingly, the majority of remaining common genes were associated with energy production through glycolysis and oxidative phosphorylation (*Eno1*, *Sdha*, *Sdhb*). Energy supply as a common function was further indicated by genes associated with lactate production (*Ldha*). Cholesterol synthesis and trafficking (*Apoe*), glutamate uptake (*Slc1a3*)

and glutamate metabolism (*Glud1*) have also been described as common astrocyte processes[1] (Figure. 3b).

However, >70% of enriched genes were specific to a subtype (Supplementary Table 3, Supplementary Files 2-4). Furthermore, only 1 gene amongst the top 10 expressed by each subtype was shared (Supplementary Table 4). Amongst differentially expressed genes, transcription factors (*Id3*, *Etv5*, *Wfs1*) were prominent, consistent with diverse transcriptional networks maintaining unique cell identities. Consistent with this, differential expression of specific genes was found across all major astrocyte functions (chosen based on a number of recent reviews)[6, 7, 29, 30, 31, 32]. These functions include synaptogenesis (*Chrdl1*, *Lrtm2*, *Sema4b*), phagocytosis (synapse removal) (*Mertk*), synapse function/plasticity (*Agt*, *Ndrg4*, *Ppp1ca*, *Dbi*, *Slc7a10*, *Glul*), neurotransmission (*Gria1*, *Gabrg1*), ion transport (*Kcnj16*, *Kcnj10*, *Kcnk1*), water transport (*Aqp4*), formation and/or maintenance of the blood brain barrier (*Mfsd2a*) and immune function (*Tril*, *Tlr3*) (Figure 3c).

Hence, our data further confirm the molecular heterogeneity of astrocytes. This heterogeneity encompasses well recognized astrocyte functions and exists both between and within brain regions.

**_In situ_ mapping of astrocyte subtype location**

Based on closer examination of RNA-seq gene lists, a set of markers was identified to specifically label astrocytes (Figure 2d), based on overall levels of gene expression (absent/low to high relative expression). These genes encoded proteins involved in cytoskeletal function (*Gfap*), membrane fusion (*Unc13c*), regulation of cerebral blood flow and synaptic transmission (*Agt*), Wnt signaling (*Frzb*), cell fate specification (*Ascl1*), post-translational protein modification (*Ogt*) and actin binding (*Fam107a*), respectively. To specifically map back astrocyte subtypes in brain tissue, we performed multiplexed fluorescence *in situ* hybridization (ISH) experiments (RNAscope) on coronal sections of adult mouse brain, using probes specific for these markers (see Methods and Supplementary Table 5).

**A unique subtype linked to neurogenesis: AST4**

Examination of genes enriched in AST4 revealed a disproportionate number of them to be involved in mitosis and cell cycle control (*Cdk4*, *Sirt2*), transcriptional regulation (*Ascl1*, *Emx1*), and neurogenesis and neuronal differentiation (*Dab1*) (Supplementary Tables 6, 7). Our initial tissue dissection also recovered the dentate gyrus of the hippocampus. Based on the high expression levels of *Frzb*, *Ascl1* and *Slc1a3* in our sequencing data, the fact that *Ascl1* is known to be expressed in neural stem cells and amplifying progenitors, and the

known staining patterns of these genes in the Allen Brain Atlas (Supplementary Figure 9), we hypothesized that AST4 represents a population of hippocampal neural stem or progenitor cells[33, 34]. Coronal sections of adult mouse brain were stained with probes against *Frzb* and *Ascl1* as subtype specific markers and *Slc1a3* as a general marker of stem cells and astrocytes[34] (Figure 4a, Supplementary Figures 10, 11). The anatomical distribution of cells expressing all three marker genes is shown in the low magnification section, using black dots to mark cells of interest. To allow a detailed description of astrocyte localization and quantification, images were manually segmented, based on definitions from the Allen Brain Atlas (Mouse Reference Atlas, Coronal). Higher magnification images confirming colocalization to individual cell nuclei are also shown, with quantification of individual fluorescence puncta per cell used as a proxy for mRNA expression levels (left hand bar plot Figure 4a and Methods). The distribution of AST4 throughout the brain was quantified in two separate ways. First, distribution through the brain was plotted, based on the number of AST4 astrocytes detected in a given region (middle plot Figure 4a). Second, the proportion of AST4 astrocytes relative to the total number of all astrocytes in each brain region was determined (right hand plot Figure 4a). As predicted, AST4 localizes predominantly to the subgranular zone in the hippocampus and forms the majority of *Slc1a3* positive cells detected in this region. This result verifies the power of our sequencing-based approach to resolve individual astrocyte subtypes, as well as our ISH-based mapping.

**A possible intermediate progenitor: AST5**

AST5 was the rarest subtype we found by Smart-seq2 sequencing (Figure 2a, Supplementary Table 2). AST5 showed considerable overlap with AST4 (Supplementary Table 3), being enriched in genes involved in mitosis and cell cycle control (*Sirt2*, *Sept2*, *Emp2* etc). However, there were also considerable differences, with AST5 being enriched for genes involved in classical astrocyte functions, such as glucose metabolism and energy production (Supplementary Tables 6 and 8), suggesting that AST5 represents an intermediate transition state between progenitors and mature astrocytes. The distribution of AST5, based on relatively high expression of *Fam107a* and low expression/absence of O*gt* (Figure 4b, Supplementary Figures 10, 11), was difficult to obtain accurately given the large variability between samples. However, based on absolute cell numbers, a trend exists towards enrichment in cortical layers 2/3 and 5. As a proportion of the *Slc1a3* positive cell population, AST5 appeared dominant in the subpial region, as well as the stratum lacunosum moleculare and dentate gyrus of hippocampus.

**Mature astrocytes: ASTs 1, 2 and 3**

In contrast, AST1, AST2 and AST3 showed gene enrichment profiles more consistent with mature astrocyte function.

AST1 is defined by high expression of *Gfap* and *Agt* and was found at high levels in the subpial layer and hippocampus - both in terms of absolute distribution and normalized to total astrocyte number (Figure 5a; Supplementary Figures 10, 12, 13). This is entirely consistent with previous reports of *Gfap* staining in the rodent brain[30] and the unique characteristics of marginal astrocytes[9, 35]. Gene enrichment and functional annotation analysis revealed only a handful of subtype overexpressed genes and related pathways (Supplementary Tables 6, 9). With reference to common astrocyte functions, however, synaptogenesis (*Nrxn1*, *Prex2* and *Plekhb1*), synaptic plasticity (*Agt)* and glutamatergic neurotransmission (*Arl6ip1*) were clearly distinct from other subtypes (Supplementary Table 9).

Based on ISH, AST2 and AST3 both showed highly reproducible and specific distribution patterns across cortical layers and hippocampus. AST2 was localized by higher than average expression of the marker gene *Unc13c* and low or absent expression of *Agt*. It was found in the highest absolute numbers in cortical layers 2/3 and 5, with lower amounts in layers 1, 4 and 6 and negligible amounts in hippocampus (Figure 5b, Supplementary Figures 10, 14). However, normalized to total astrocyte number per region, AST2 appears uniformly distributed across cortical layers. The distribution of AST3 was predicted by expression of *Agt* and little or no expression of *Unc13c* and *Gfap*. The limited number of spectral channels available to us at the time using RNAscope (3 markers including *Slc1a3*) meant we had to adopt a split-staining approach, performing 2 different sets of staining: the first for *Gfap*, *Agt* and *Slc1a3* (Figure 6a) and a second for *Unc13c*, *Agt* and *Slc1a3* (Figure 6b). Both showed AST3 distributed throughout the cortex and hippocampus (see also Supplementary Figures 10, 12, 13, 14). Based on the high levels of AST1 localizing to the pial layer and stratum lacunosum-moleculare (SLM) in hippocampus (Supplementary Figure 12), we anticipate it being the dominant subtype in these regions. Considering the heavy *Gfap* staining, and the split staining approach taken for AST3, we expect that the overall levels of AST3 are relatively low in these two regions (Figure 6a versus Figure 6b). It is possible that AST2 also follows a similar distribution pattern in the cortex, and is found in lower amounts in the pial region, as *Gfap* expression is also low in AST2 (Figure 2). RNAscope stainings across multiple tissue sections (Supplementary Figure 10) suggest a substantial degree of intermixing between these two cell types in mid-cortical layers, while AST3 appears to be the dominant subtype in layer 6. In this respect, it is interesting that the two subtypes show differential gene enrichment profiles for processes relating to synaptic function (AST2, glutamatergic transmission, *Slc7a10*, *Gria2*; AST3, GABAergic transmission, *Gabrg1*) and synaptogenesis and process outgrowth (AST2, *Slitrk2*, *Sema4b*; AST3, *Etv5*, *Spon1*), suggesting differential regulation of functions by these subtypes (Supplementary Table 9).

For ease of interpretation, we have summarized the complex spatial relationships between subtypes schematically (Figure 7).

**Morphological correlates of identified astrocyte subtypes**

Distinct transcriptomic profiles and spatial locations for astrocyte subtypes predict morphological and functional specialization[7]. Unfortunately, with the exception of *Gfap*, the markers exploited for subtype identification currently have a limited range of molecular reagents available (GFP-marker mice, specific Cre-lines, antibodies etc.) to facilitate further such experiments. However, our ISH-based mapping showed that subtypes are differentially distributed across cortex and hippocampus. Therefore, we used an alternative strategy to investigate these issues, based on the sampling of large numbers of astrocytes in specific brain regions. Our rationale was that by taking this approach we could correlate the presence of distinct morphologies or functional characteristics to the spatial patterning of our molecular subtypes. Given the limitations of our approach, we decided to focus on regions containing ASTs 1, 2 and 3, as these subtypes most likely represent mature astrocytes.

Previous studies on astrocyte morphology have given variable results, presumably due to the labeling methods used. Hence, we examined recent studies in which either regional or sub-regional differences were measured, using methods that gave high astrocyte coverage in adult C57/Bl6 mice[9, 36].

Astrocytes positioned in cortical layers 2-4 (which contain AST2 and AST3) display a smaller territorial volume and arborization than astrocytes in the hippocampal CA3 region (containing AST3), as judged by Golgi staining and immunohistochemistry for the astrocyte marker S100β[36].

Cortical astrocytes, labeled using genetically encoded marker proteins, show differences in arborization, territorial volume and cell orientation through layers 1-6[9]. These became more apparent using a hierarchical clustering of 5 key morphological parameters (including elongation, flatness, and various measures of cell orientation)[9]. Using this approach, the authors identified four prominent morphological subtypes (A-D), which distribute through the various cortical layers in differing proportions[9], consistent with data from our ISH experiments (Figures 4-6). Of note, there is a correlation between the morphologies identified and the molecular subtypes we report. Marginal astrocytes (AST1) showed a substantial similarity to Cluster D, given their unique morphology and localization in the pial layer[9, 37]. Cluster B was present in cortical layers 1-6, while Cluster C was present in cortical layers 2-5, with lower proportions in layers 1 and 6. These distributions show remarkable similarities to those of AST3 and AST2, respectively. However, Cluster A was restricted to layers 5 and

6, suggesting that the correspondence between transcriptome and morphology is incomplete (see below).

**Physiological correlates of identified astrocyte subtypes**

Astrocyte activation is commonly associated with a transient rise in intracellular $Ca^{2+}$, which has been linked to functional outputs[6]. Hence, heterogeneity in $Ca^{2+}$ signaling has been proposed as a mechanism by which astrocytes execute diverse functions[6]. We investigated the possibility of differential astrocyte $Ca^{2+}$ signaling using acute coronal tissue slices, in which cells were labeled with the $Ca^{2+}$ indicator Fluo-4, and co-labeled with sulforhodamine 101 (SR101) for astrocyte identification. Images were acquired using a 2-photon microscope in cortical layer 1, cortical layers 3-5 and hippocampal CA1. Cell activity was measured under three consecutive conditions. Baseline (BASE) reflects astrocyte activity when neurons were spontaneously active. Application of Tetrodotoxin (TTX) was then used to block neuronal activity, isolating astrocytes from the influence of local neuronal network activity. Finally, phenylephrine (PHE) was applied to tetrodotoxin-treated slices to directly trigger robust $Ca^{2+}$ responses in astrocytes[38], independent of neuronal activity (Figure 8a). Only cells responding to PHE were retained for analysis (Figure 8b) and profiles showing changes in intracellular $Ca^{2+}$ were plotted as fractional fluorescence changes relative to baseline ($dF/F_o$) (Figure 8a). While we observed significant differences in activity between astrocytes across regions in baseline and TTX conditions, the most striking differences were seen after application of PHE (Figure 8c).

In order to eliminate potential bias, caused by manual assignment of cells to brain regions, we performed unbiased hierarchical clustering of astrocytes, based on the various $Ca^{2+}$ peak parameters recorded following PHE application (Figure 8d, e). We identified 3 distinct clusters of astrocytes, which were differentially distributed through cortical layers 1 and 3-5, as well as hippocampal CA1. Cluster 2 was mostly comprised of cortical astrocytes from layer 1 and layers 3-5. In contrast, hippocampal astrocytes were a minority. Based on comparisons to our ISH data, it is likely that Cluster 2 contains a mixture of AST1 and AST2, which are located in the cortex. Cluster 3 contained roughly equal quantities of astrocytes from across brain regions, consistent with cells having an AST3 identity. Interestingly, Cluster 1 was mostly composed of hippocampal CA1 astrocytes, and is likely comprised of AST3, indicating the potential for further axes of heterogeneity, such as local environment, to also influence cell identity (see below). Significant differences across clusters were seen for the measured signal parameters (Figure 8f).

Taken together, these data indicate that molecularly defined astrocyte subtypes share overlapping spatial locations with cells possessing distinct morphologies and physiological responses.

## DISCUSSION

Astrocytes have been reported to play many diverse roles in the CNS, such as synapse formation and elimination, maintenance of local homeostasis and modulation of synaptic transmission[1]. However, whether astrocytes are functionally specialized to perform certain tasks remains unclear. This is despite evidence supporting the formation of local specialized neuronal microcircuits, in areas such as visual cortex[39] and hippocampus[40].

To measure diversity both between and within brain regions, we used a single cell sequencing approach in adult tissues to achieve an unbiased view of astrocyte heterogeneity, free of possible interference from transcriptional programs related to CNS development[5]. Our results distinguish multiple astrocyte subtypes at the transcriptomic level. However, the picture is substantially more complicated than for neurons, with little clear evidence for distinct cellular hierarchies in clustering, most likely due to multiple axes of heterogeneity being present[4, 5, 20, 41]. However, while astrocyte subtypes share common genes associated with core functions, the transcriptomic differences between the subtypes are still sufficiently large to suggest distinct specializations in known astrocyte functions[13, 42]. This is reinforced by our ISH results. Differential localization through hippocampus and cortex supports the concept of local astrocyte diversity, while consistency across sections from multiple animals indicates the subtypes identified are genuine and not transient cell states. As we performed analysis on sections cut to maximize the cross-sectional area of cortex and hippocampus for imaging (Supplementary Figure 10), we cannot discount variations in spatial distribution along the rostro-caudal axis. However, as the cells recovered for sequencing were obtained from whole cortex and hippocampus, we are confident the overall subtype distribution will largely reflect this fact.

The observation of unique transcriptomic profiles and spatial patterning suggests several intriguing possibilities, including links between cortical and hippocampal astrocyte populations. Astrocyte generation from distinct progenitors in mouse brain and spinal cord has been proposed, in which broad sections of CNS are populated by astrocytes derived from progenitors of fixed developmental origin[43, 44]. For example, the widespread distribution of AST1 and AST3 across cortex and hippocampus hints at a common developmental origin from embryonic pallium[45] (Supplementary Figure 15). Furthermore, AST5 possesses a unique transcriptome, which appears to be intermediate between a progenitor (AST4) and a mature astrocyte (AST1) (Supplementary Tables 3, 4, 6-9), consistent with the proposed

concepts of cortical astrocyte formation from local proliferation of common progenitors followed by non-synchronous maturation[46, 47, 48].

The relationship between AST2 and AST3 remains unclear at present, although a number of possibilities exist. These subtypes could be formed from a common class of progenitor, defined by early patterning events and diversified by cues from neighboring CNS cells, such as neuronal release of sonic hedgehog (Shh)[49, 50]. Alternatively, they may be formed from distinct classes of progenitor, which intermix in the cortex[51]. However, in this latter scenario it is interesting to note that the morphological development of clonally-related astrocytes also appears to be strongly influenced by local environment[51]. A potential role for signals commonly associated with development (such as Shh signaling) is interesting, as evidence suggests that persistent activation of these pathways is necessary to maintain astrocyte diversity[52]. In this respect, it is not surprising that genetic ablation of neuronal *vglut1* has been reported to adversely affect postnatal development of cortical astrocytes[53]. In fact, AST2 and AST3, which are found throughout cortex, differentially express genes involved in neurotransmission. AST2 is enriched in transcripts linked to glutamatergic neurotransmission (including *Slc7a10*, which is involved in mobilization of the potent NMDA agonist D-serine[54]); in contrast AST3 is enriched in transcripts associated with GABAergic neurotransmission. This suggests that reciprocal interactions between astrocytes and neurons may promote functional diversity at the local circuit level[39, 40]. Consistent with this, a recent study on the role of astrocytes in glutamatergic synapse maturation in cortex identified astrocyte-secreted Chordin-like 1 (*Chrd1*)[42] as an essential factor stabilizing synapses, which we find enriched in AST2. In this respect, comparative studies on the synaptogenic action of Norrin (*Ndp*) (present in ASTs 2 and 3) may prove instructive[13]. Furthermore, genetic manipulations, such as neuronal deletion of *Dab1*[9] or *Satb2*[41] also influence astrocyte positioning.

Recent years have seen a rapid growth in single cell CNS studies[4, 5, 20, 55]. These studies generally report transcriptomic differences between astrocytes originating from different brain regions or, in the case of cortex, an approximate separation in gene expression between layer 1 and the remaining layers. (A detailed comparison between studies is made in Supplementary Figure 16). In contrast, our results point towards a greater degree of intra-regional heterogeneity in the adult mouse brain. The possible causes for this discrepancy are unclear at present, but are likely related to methodological issues (such as age of animals used[4, 20, 55], mRNA detection sensitivity[4, 5, 20, 55, 56] etc.). However, we are confident that our results provide an accurate survey of astrocyte subtypes present in both cortex and hippocampus of adult mouse brain. Sequencing several hundred cells for optimal coverage resulted in robust clustering of ASTs 1-4 (Supplementary Figure 17). Only in the case of

AST5, which is the rarest subtype we identified, do we consider that sequencing more cells could possibly reveal greater diversity. Furthermore, our results largely recapitulate earlier findings, produced using a variety of cell capture technologies and sequencing techniques, such as the differential expression of *Gfap* and *Mfge8* between upper and deep cortical layers[4, 20] (Supplementary Figure 18). Furthermore, they show that markers previously reported for cortical (*Igfbp2, Sparc*)[5] and hippocampal (*Nnat, Fabp7*)[5] astrocytes are differentially expressed between ASTs 1-5 (see Supplementary Figure 19 and online resource), suggesting that the optimized protocols used in our study actually allow for a more subtle characterization of cells.

The robustness of our data is demonstrated by consistency with a study from Bayraktar and colleagues[41], which uses large-scale ISH-based mapping to study gene expression in somatosensory cortex of P14 mice (see Supplementary Figure 19). In both studies, there was considerable overlap between astrocyte gene expression and spatial mapping. For example, *Id3*+ astrocytes mapped to layer 1 (AST1), *Chrdl1*+ astrocytes mapped to the middle cortical layers (AST2) and *Il33*+ astrocytes were found over-represented in layers 5 and 6 (AST3). Although there were some differences, these could be explained by the age of the animals used[48], or by differences in the methodologies employed.

Tissue dissociation has been reported to induce transcriptional changes[57]. However, the close correlation between our *in silico* analysis and ISH validation suggests this is of limited concern in our study, possibly due to the fact that we used a rapid one step isolation procedure run at low temperature (wherever possible). Another major concern with FACS use is tissue integrity and the loss of fine astrocyte processes (Supplementary Figure 5a)[58]. Although some mRNAs in astrocytes are actively transported into processes for local translation[58] this does not mean that those mRNA species will be absent from the soma. In fact, work in neurons has shown that there is no known case of a mRNA produced in the nucleus that is localized exclusively outside the cell body. Extrapolating on this, we expect sequencing the content of the soma to reflect the vast majority of the mRNAs expressed by an astrocyte[59].

Our work provides a detailed characterization of astrocyte transcriptomic diversity and additional evidence that this can be linked to cell morphology[9, 10] and differential $Ca^{2+}$ signaling[10]. However, there are issues that need to be resolved. For example, a proportion of astrocytes in cortical layer 6, which correlate to AST3, appear to have a distinct morphology[9]; the mechanisms underlying this unique specialization, such as local tissue architecture and signaling[52], require further investigation. Given the complex molecular

fingerprints of the subtypes we identified, such experiments will require the development of specific labeling techniques, based on intersectional genetics[60].

In summary, we have demonstrated both inter- and intra-regional heterogeneity of astrocytes and have shown distinct cortical layering and hippocampal compartmentalization of these unique subtypes. Furthermore, we provide evidence that these subtypes possess distinct morphologies and physiologies. This work provides a highly resolved roadmap for future investigations of astrocyte heterogeneity. Freely available as an online resource, our data allows development of testable hypotheses relating to astrocyte properties, that will ultimately allow their effects on CNS form and function to be elucidated. Such information will prove invaluable to our overall understanding of brain activity in both healthy and diseased states.

## METHODS

**Animal experiments.** All experiments were approved by the Ethical Research Committee of the KU Leuven and were in accordance with the European Communities Council Directive of 22 September 2010 (2010/63/EU) and with the relevant Belgian legislation (KB of 29 May 2013). C57BL/6J mice were used throughout. Mice aged to post-natal (P) day 56 were used for single cell RNA-seq. Male mice aged to P56-P60 were used for *in situ* hybridization experiments. Both male and female mice aged to P40-P67 were used for $Ca^{2+}$ imaging experiments.

**Preparation of a single cell suspension.** Cortical and hippocampal astrocytes were prepared independently, at roughly equivalent circadian times. Two separate batches of astrocytes, originating from each region, were prepared, using multiple litters of mice. Cortical astrocytes were isolated from litter number 1. Hippocampal astrocytes were isolated from litter numbers 2 and 3.

Briefly, regions of interest (cortex and hippocampus) were quickly and carefully dissected in cold HBSS buffer without $Ca^{2+}$ and $Mg^{2+}$ (Sigma-Aldrich), under a binocular microscope. Myelinated parts were discarded, to decrease the amount of debris in the final cell suspension. Cortical cell suspensions were prepared from two littermate animals in parallel using separate tubes. Two hippocampal cell suspensions were also prepared in parallel using separate tubes; in this case, two different sets of four littermate animals were used. Tissue dissociation was run using the neural tissue dissociation kit (P) (Miltenyi Biotec)[25]. Tissue was digested at 37°C using papain, supplemented with DNAse I. Tissue was mechanically dissociated using three rounds of trituration with 5 ml serological pipettes. The resulting suspension was then filtered through a 20 μm Nitex mesh (SEFAR) to remove any remaining clumps. Contamination by myelin and cell debris was removed by equilibrium density centrifugation. 90% Percoll PLUS (Life Sciences) in 1x HBSS with $Ca^{2+}$ and $Mg^{2+}$ (Sigma-Aldrich) was added to the suspension to produce a final concentration of 24% Percoll. Additional DNAse I (Worthington) was added (125 U per 1 ml), before the cell suspension was centrifuged at $300g_{Av}$ for 11 minutes at room temperature (with minimal centrifuge braking). The resulting cell pellet was resuspended in dPBS (without $Ca^{2+}$/$Mg^{2+}$) containing 0.5% BSA (Sigma-Aldrich). Supernatants were centrifuged again at $300g_{Av}$ for 10 min at room temperature. Any pelleted cells were resuspended in 0.5% BSA/dPBS (without $Ca^{2+}$/$Mg^{2+}$). Cells were pooled and FACS sorted.

**FACS isolation of astrocytes.** All steps were performed at 4°C. Cells were incubated with FcR blocking reagent (Miltenyi Biotec) at a 1:9 dilution for 10 min to block non-specific binding of antibodies. This was followed by addition of antibodies specific to the cell

isolation protocol. ACSA-2-PE antibody (Miltenyi Biotec, 130102365) (1:140 dilution) and O1-eFluor660 (eBioscience, 50-6506-80) (1:810 dilution) were added to the cell suspension and incubated for 10 min. 0.5% BSA/dPBS (without $Ca^{2+}$/$Mg^{2+}$) was then added to the cell suspension as a washing step. Cells were recovered by centrifugation at $300g_{Av}$ for 10 min. The resulting pellet was then resuspended in 0.5% BSA/dPBS and filtered through a 20 µm Nitex mesh. The vital dye 7-AAD (eBioscience, 00-6993) (1:100 dilution) was added to exclude dead cells during FACS.

FACS was performed on a BD FACSAria III using a 100 µm nozzle. Compensations were done on single-color controls and gates were set on unstained samples. Forward Scatter (FSC)/Side Scatter (SSC) gatings were used to remove clumps of cells and debris. Single ACSA-2-PE-positive/O1-eFluor660-negative/7-AAD-negative astrocytes were sorted into separate wells of non-skirted 96 well PCR plates (VWR). Each plate also contained 1 well without any cell(s) (negative control), 1 well with 40 astrocytes (positive control: astrocytes) and 1 well with 40 7-AAD-negative cells (positive control: viable cells). Each well contained 4.3 µl of lysis buffer composed of 2.3 µl 0.2% Triton X-100 (Sigma-Aldrich) with 2 U $\mu l^{-1}$ RNase inhibitor (Clontech), 1 µl of HPLC-purified 10 µM Oligo-dT30VN oligonucleotide (AAGCAGTGGTATCAACGCAGAGTAC$T_{30}$VN) and 1 µl of dNTP mix (Fermentas). Plates were kept at 4°C during the sort, sealed immediately afterwards, vortexed and spun down at $300g_{Av}$ for 30 s. Plates were stored at -80°C until library preparation.

**Single cell cDNA and library preparation.** We used a modified Smart-seq2[21] protocol. Briefly, samples were reverse transcribed. ERCC (External RNA Controls Consortium) control RNAs (Thermo Fisher Scientific) were added into the reverse transcription mix at a final dilution of $1:160x10^6$. TSO (template switching oligonucleotide) (AAGCAGTGGTATCAACGCAGAGTACATrGrG+G in which the last guanosine is a locked nucleic acid: LNA) was used at 0.2 µM in the final reaction mix. Subsequent preamplification of cDNA used an ISPCR oligonucleotide (AAGCAGTGGTATCAACGCAGAGT) and 22 PCR cycles. cDNA was purified from the PCR mix using Agencourt Ampure XP beads (Beckman Coulter) with a modified bead:DNA ratio of 0.8 to 1. The quality of cDNA was checked by analyzing 11 single cell libraries from each 96 well plate using a NGS Fragment High Sensitivity Analysis Kit (Advanced Analytical) and a Fragment Analyzer (Advanced Analytical). Data were analyzed using PROSize 2.0 software. The cDNA concentration was measured in every well using a Quant-iT PicoGreen dsDNA Kit (Invitrogen), using a standard protocol. A Synergy 2 plate reader controlled by Gen5 software (BioTek) was used to measure fluorescence.

Libraries were prepared using a Nextera XT DNA Library Preparation Kit (Illumina) with 4 sets of Nextera XT v2 index kits (sets A to D) (Illumina FC-131-2001 to FC-131-2004), using a standard protocol with minor modifications. Tagmentation was run on 0.125 ng cDNA (adjusted to a final volume of 1.25 µl) in a reaction mixture containing 2.5 µl Tagment DNA buffer and 1.25 µl of Amplicon Tagment Mix. This was followed by PCR amplification of adapter-ligated fragments, using a reaction mix consisting of 6.25 µl of Tagmentation product, 3.75 µl of Nextera PCR Master Mix and 1.25 µl of each Index primer (N7xx and N5xx). PCR was run using a standard program consisting of 12 cycles. Libraries prepared with 4 different sets of index kits were then pooled and cleaned using Agencourt Ampure XP beads (Beckman Coulter). DNA was mixed with beads at a 1:0.6 ratio. Following an 8 min incubation, beads were recovered using a magnetic stand, supernatant was removed and beads were washed twice with 80% ethanol. Beads were then dried for 10 min before DNA was eluted in 50 µl of EB buffer (Qiagen). Bead purification was repeated a second time using a 1:1 DNA:bead ratio. Size distribution of library pools was checked using a Fragment Analyzer and a NGS Fragment High Sensitivity Analysis Kit, according to standard protocols (Supplementary Figure 5). Library pools were sequenced (75 bp paired-end reads) using a NextSeq 500 system (Illumina) and a NextSeq 500/550 High Output Kit v2 (150 cycles) (Illumina). Libraries were sequenced on average to a depth of 1M reads per library.

**Analysis of RNA sequencing data.** An initial quality check of sequenced libraries was undertaken using FASTQC 0.11.4 software. STAR 2.5.2b software was used to map sequencing reads against Release M12 (GRCm38.p5) of the mouse reference genome (Gencode), modified to take ERCC sequences (https://assets.thermofisher.com/TFS-Assets/LSG/manuals/cms_095047.txt) into account. Unique read maps were identified using STAR, after the removal of non-canonical unannotated junctions and non-canonical unannotated introns (using software specific parameters). Output alignment BAM files were then merged and sorted using Samtools version 1.4. RNA quality metrics were collected with Picard Tools version 1.140. Gene counts were generated using HTSeq version 0.6.1p1.

Clustering was done with Seurat version 1.4.0.16, run on RStudio version 1.0.136, using R version 3.4.0. Data was ln-normalized using the default Seurat method. 16 cells out of 2,031 that passed FASTQC and additional quality measures (Supplementary Figure 7) were discarded at this point, as they did not pass the minimal total expression threshold of 54 transcripts. High level cell type identification was performed with a starting base of 24,761 genes expressed across 2,015 samples. 5,455 highly variable genes (ln-mean expression > 0.3 and ln-variance/mean > 0.1) were identified and used for clustering with the default Seurat pipeline. After discarding all other higher order cell types, astrocytes were reclustered using the default Seurat method. Analysis was performed based on the expression of 13,087 unique

genes across 1,811 astrocytes. 886 highly variable genes (ln-mean expression > 0.5 and ln-variance/mean > 0.5) were identified and used for clustering. Unless stated, subsequent identification of genes overexpressed in the astrocyte subtypes, including specific marker genes, was also performed using the default Seurat pipeline. Genes were identified using a number of criteria. First, only significantly up-regulated genes ($p < 0.01$) were considered. Second, genes had to be at least 1.28-fold overexpressed in the subtype of interest (when compared to all other astrocytes). This number was empirically chosen to give the best compromise between the number of marker genes identified in each subtype (allowing functional annotation) relative to background noise. Finally, markers had to be expressed in more than 25% of the cells identified as belonging to a particular subtype. These marker genes were further used for gene-enrichment and functional annotation analysis. Note that the AST2 marker *Unc13c* was found using the default PAGODA (R Scde 1.99.1 package) differential gene expression analysis pipeline[61]. It has a ln-mean expression of 0.28, and a ln-variance/mean of 0.41. Although it was not considered in our Seurat analysis, it remains the marker of choice for AST2, due to its remarkably high specificity.

To exclude a dominant role of batch effects in cluster analysis, extensive controls were performed and can be found in Supplementary File 1 and online at https://holt-sc.glialab.org/.

Gene-enrichment and functional annotation analysis (GO, KEGG and BioCarta) of subtype overexpressed genes were performed using DAVID[27] version 6.8. All genes detected in astrocytes (13,087) were used as the background gene set. Only pathways with $p$ values < 0.1 (EASE score; modified Fischer's Exact Test) were taken into consideration. Additionally, only pathways with $p < 0.5$ (Benjamini-Hochberg test; false discovery rate (FDR) correction) were analyzed.

Genes identified as overexpressed in specific subtypes were also manually curated with the UniProt database (https://www.uniprot.org/)[28] for assignment of putative gene functions.

**RNAscope fluorescence *in situ* hybridization.** RNAscope (Advanced Cell Diagnostics; ADC) was performed as follows. Briefly, brains were quickly frozen in Optimum Cutting Temperature (OCT) compound (Tissue-Tek), using isopentane chilled with liquid nitrogen. 10 µm brain slices were prepared using a NX70 cryostat (Thermo Fisher Scientific). Sections were subsequently fixed in ice-cold 4% PFA for 30 min. Sections were then dehydrated using a series of ethanol solutions (50% - 100%), before drying and incubating with Protease IV for 20 min at room temperature. Slides were washed in PBS and hybridized with gene specific

probes (Supplementary Table 5) for 2 h at 40°C in a HybEZ Oven (ACD). Non-annealed probes were removed by washing sections in 1x proprietary wash buffer. Probes were then detected via sequential hybridization of proprietary amplifiers and labeled 'secondary' probes (Amp 1 – Amp 4). Finally, sections were stained with DAPI and mounted using ProLong Diamond Antifade Mountant (Life Technologies).

**Imaging and data analysis.** Brains were imaged using an Axio Scan Z1 microscope (Zeiss), operated by Zen 2.3 software (Zeiss). Images were acquired using standard excitation and emission filters. Images were taken in the best focal plane using a PL APO20x/NA 0.8 objective or a PL APO40x/NA 0.8 objective. Images were exported as separate TIFF files and imported into NIS-Elements software (version 5.02.00) (Nikon) for further analysis. Brain regions were defined according to the Allen Brain Atlas and were manually superimposed onto the images. Cells were defined as polygons centered on DAPI spots: each polygon had an average size ~1.3 times larger than that of the DAPI signal. Individual bright spots of fluorescence (signals higher than a background threshold) within these boundaries were counted as individual mRNA transcripts. Astrocytes were defined by expression of the pan astrocytic marker *Slc1a3* (coding for GLAST). Astrocyte subtypes were identified based on colocalization of specific marker genes. Data for each specific astrocyte subtype was collected from coronal sections generated from at least 3 independent animals. Robustness of the subtype distribution was checked by varying the fluorescence thresholds used to define transcripts across a range of intensities.

**Preparation of acute brain slices**. Preparation followed a published protocol[62] and was performed as follows. Animals were anaesthetized using intraperitoneal administration of Nembutal (50 mg/kg). Transcardial perfusion was performed using 20 ml of ice-cold N-Methyl-D-glucamine (NMDG)-based artificial cerebrospinal fluid (NMDG-ACSF) dissection solution, containing (in mM): NMDG 93, KCl 2.5, $NaH_2PO_4$ 1.25, $NaHCO_3$ 30, $MgSO_4$ 10, $CaCl_2$ 0.5, HEPES 20, D-glucose 25, L-ascorbic acid 5, thiourea 2, sodium pyruvate 3, N-acetyl-L-cysteine 10; pH 7.4 (HCl). Osmolarity was adjusted to 305-310 mOsm/l if needed. The solution was bubbled in 95% $O_2$/5% $CO_2$ gas for twenty minutes before use and bubbling was maintained throughout the experiment. Following decapitation, the brain was swiftly removed. 350 μm thick coronal slices, containing the posterior cortex and/or dorsal hippocampus, were obtained using a Leica VT1200s vibratome. Slices were further hemisected and placed in a chamber containing NMDG-ACSF maintained at 33ºC. Slices were maintained under these conditions for 25 min, with the controlled reintroduction of $Na^+$ achieved by gradual addition of 2M NaCl to the chamber. Slices were then transferred to another chamber containing room temperature standard ACSF (in mM) NaCl 124, KCl 4.5, $NaH_2PO_4$ 1.25, $NaHCO_3$ 26, $MgCl_2$ 1, $CaCl_2$ 2.5, D-Glucose 10; pH 7.4 (HCl); 95% $O_2$/5%

691 $CO_2$ gas; osmolarity 305-310 mOsm/l. Slices were removed and transferred to a 6 well plate
692 for loading with dyes (see below), before being returned to the chamber. For imaging, slices
693 were transferred to a specialized recording chamber and superfused with normal ACSF
694 (including pharmacological reagents where appropriate) at 33°C with a flow rate of 2 ml/min.

695

696 **Preparation and application of pharmacological reagents.** Stock solutions were prepared
697 using dd$H_2O$ and stored as frozen aliquots. Final working solutions were produced from
698 thawed aliquots by dissolving at least 1000-fold in normal ACSF. Tetrodotoxin citrate (TTX,
699 Tocris Biosciences) was used at a final concentration of 1 µM. (R)-(-)-Phenylephrine
700 hydrochloride (PHE, Tocris Biosciences) was used at a final concentration of 50 µM.

701

702 **Astrocyte identification and calcium imaging.** To identify astrocytes, cells were labelled
703 with SR101. To avoid potential issues associated with high levels of SR101 loading (such as
704 induction of seizure like activity)[63], slices were incubated for 20 min in a 6 well culture dish
705 containing 1 µM SR101 (Sigma-Aldrich) in ACSF at 33ºC. Labeling of cells appeared
706 homogeneous, as judged by visual inspection, with the possible exception of cortical layer 1,
707 which is likely due to its high astrocyte density[64]. Following SR101 labeling, slices were
708 moved to another well for loading with the calcium indicator Fluo4-AM. The dye was
709 supplied as a 50 µg ampoule (Thermo Fisher Scientific) and was solubilized using a mixture
710 of 7 µl DMSO, 2 µl 20% Pluronic F-127 in DMSO (Tocris Biosciences) and 1 µl 0.5%
711 Kolliphor EL (Sigma-Aldrich) in DMSO. The ampoule was then incubated at 41ºC with
712 constant agitation (1,400 RPM) for 15 min using a thermomixer. Concentrated Fluo-4AM
713 was then added to the ACSF in the well, giving a final concentration of 15.2 µM. Slices were
714 loaded for 45 to 60 min at 35°C. At the end of this period, excess AM dye was removed by
715 washing in room temperature ACSF for at least one hour. Prior to use, slices were maintained
716 as described above.

717

718 All recordings followed the same protocol. First, a field of view containing either layer 1 of
719 the cortex**,** layers 3 to 5 of the cortex, or region CA1 of the hippocampus, was chosen. Each
720 field of view was recorded under three sequential conditions. First, baseline activity was
721 recorded. Next, ACSF containing TTX was bath applied for 5 min before additional imaging.
722 Finally, ACSF containing TTX and PHE was then added with further imaging. Signals were
723 recorded over a period of 300 s for each condition.

724

Live imaging of cells in acute slices was performed using a 2-photon imaging system (VIVO 2-Photon platform, Intelligent Imaging Innovations GmbH), equipped with a tunable multiphoton laser (MaiTai laser, Spectra-Physics). Imaging was performed using a Zeiss Axio Examiner Z1, equipped with a W Plan-Apochromat 20x/NA 1.0 objective. To excite both SR101 and Fluo-4, the excitation wavelength was tuned to 820 nm. Signals were detected using two fast-gated GaAsP PMTs (Hamamatsu Photosensor Modules H11706). Images were 512x512 pixels in size and acquired at a frequency between 1.8 to 4 Hz. Acquisition was controlled using Slidebook 6 software (Intelligent Imaging Innovations GmbH). Laser power was limited to a maximum of 25 mW at the specimen. The focal plane used was usually 30-100 μm within the slice.

**Image analysis.** Images were initially processed using Fiji software with standard plugins to correct for image drift and noise. Regions of interest (ROIs), comprising the cell body plus proximal processes (when visible), were superimposed onto the images. The average fluorescence for each ROI per frame was measured and exported to MATLAB (The Mathworks), using custom-written scripts. Relative variations in intracellular $Ca^{2+}$ were estimated as changes in Fluo-4 signal over the baseline (essentially $dF/F_0$). Baseline ($F_0$) was defined for each ROI to be the average fluorescence over the first 100 s of each recording. To measure $Ca^{2+}$ transient parameters, we wrote custom scripts based mainly on the MATLAB function 'findpeaks'. $Ca^{2+}$ signals (peaks) were detected and their parameters measured, using the following thresholds: peaks were isolated when $dF/F_0$ was higher than 1.15, events had a minimal width of 2 s and there was a minimal separation between peaks of 1 s. The minimal prominence of a peak compared to its neighbors was set at 0.1 $dF/F_0$. Only cells that responded to PHE were kept for analysis. This allowed us to define for each peak: the amplitude (defined as the maximum $dF/F_0$ reached in the isolated peaks), peak time (the time at which the maximum amplitude of a given peak occurred), peak prominence (the amplitude of the peak over and above that of the closest neighboring peaks) and peak width (the width of the peak at the half height of the prominence). Reported values are averages per cell per treatment. We also measured the peak frequency, defined as the number of peaks per second (Hz) and the area under the curve (AUC), using MATLAB functions, for each cell under each recording condition. All the data can be found in Supplementary File 5.

Further analysis was performed using RStudio 1.2.1335 running on R version 3.6.0. For baseline and TTX conditions, only astrocytes showing at least one $Ca^{2+}$ transient during recordings were retained for analysis. Clustering and tSNE-based dimensionality reduction were performed on the $Ca^{2+}$ transient parameters listed previously. Data was scaled and centered before tSNE analysis or hierarchical clustering. In the case of hierarchical

clustering, the optimal number of clusters was determined using the silhouette width method, followed by visual inspection to identify the major branches of the tree. Statistical tests were performed on raw data (without scaling and centering). Normality was checked using a Shapiro-Wilk test. As the data was not normally distributed, a Kruskal-Wallis test was used to identify significant differences. A *post-hoc* Dunn's test was performed to identify pairs of measurements that differed significantly, with multiple comparison *p*-values adjusted using the Benjamini-Hochberg method. For analysis purposes, data was compared between brain regions under the same experimental conditions.

**Figure preparation**. Figures were prepared using Inkscape 0.92.2, GIMP 2.8.22, Adobe Photoshop CS6 13.0.1 and Adobe Illustrator CS6 16.0.3.

## DATA AVAILABILITY

An easily searchable database for ISH and single cell data generated in this study is available online at https://holt-sc.glialab.org/sc/

The full list of common genes, markers, DAVID analysis, sequencing count table (not normalized) and metadata are provided online as Supplementary Files, as is data from the $Ca^{2+}$ imaging experiments.

Raw sequencing data are publicly available through the GEO database (GSE114000), accessible at https://www.ncbi.nlm.nih.gov/geo/query/acc.cgi?acc=GSE114000

## REFERENCES

1. Barres BA. The mystery and magic of glia: a perspective on their roles in health and disease. *Neuron* **60**, 430-440 (2008).

2. Ramón y Cajal S. *Histology of the Nervous System of Man and Vertebrates*. Oxford University Press (1897).

3. Khakh BS, Deneen B. The emerging nature of astrocyte diversity. *Annu Rev Neurosci* **42**, 187-207 (2019).

4. Zeisel A, *et al.* Molecular architecture of the mouse nervous system. *Cell* **174**, 999-1014 e1022 (2018).

794 5. Saunders A*, et al.* Molecular diversity and specializations among the cells of the adult
795 mouse brain. *Cell* **174**, 1015-1030 e1016 (2018).

796 6. Khakh BS, Sofroniew MV. Diversity of astrocyte functions and phenotypes in neural
797 circuits. *Nat Neurosci* **18**, 942-952 (2015).

798 7. Ben Haim L, Rowitch DH. Functional diversity of astrocytes in neural circuit regulation.
799 *Nat Rev Neurosci* **18**, 31-41 (2017).

800 8. Cahoy JD*, et al.* A transcriptome database for astrocytes, neurons, and oligodendrocytes: a
801 new resource for understanding brain development and function. *J Neurosci* **28**, 264-278
802 (2008).

803 9. Lanjakornsiripan D*, et al.* Layer-specific morphological and molecular differences in
804 neocortical astrocytes and their dependence on neuronal layers. *Nat Commun* **9**, 1623 (2018).

805 10. Chai H*, et al.* Neural circuit-specialized astrocytes: transcriptomic, proteomic,
806 morphological, and functional evidence. *Neuron* **95**, 531-549 e539 (2017).

807 11. Boisvert MM, Erikson GA, Shokhirev MN, Allen NJ. The aging astrocyte transcriptome
808 from multiple regions of the mouse brain. *Cell Rep* **22**, 269-285 (2018).

809 12. Morel L*, et al.* Molecular and functional properties of regional astrocytes in the adult
810 brain. *J Neurosci* **37**, 8706-8717 (2017).

811 13. Miller SJ*, et al.* Molecularly defined cortical astroglia subpopulation modulates neurons
812 via secretion of Norrin. *Nat Neurosci* **22**, 741-752 (2019).

813 14. John Lin CC*, et al.* Identification of diverse astrocyte populations and their malignant
814 analogs. *Nat Neurosci* **20**, 396-405 (2017).

815 15. Morel L*, et al.* Intracortical astrocyte subpopulations defined by astrocyte reporter mice
816 in the adult brain. *Glia* **67**, 171-181 (2019).

817 16. Zamanian JL*, et al.* Genomic analysis of reactive astrogliosis. *J Neurosci* **32**, 6391-6410
818 (2012).

819 17. Itoh N*, et al.* Cell-specific and region-specific transcriptomics in the multiple sclerosis
820 model: focus on astrocytes. *Proc Natl Acad Sci U S A* **115**, E302-E309 (2018).

821 18. Yeh TH, Lee DY, Gianino SM, Gutmann DH. Microarray analyses reveal regional
822 astrocyte heterogeneity with implications for neurofibromatosis type 1 (NF1)-regulated glial
823 proliferation. *Glia* **57**, 1239-1249 (2009).

824 19. Kelley KW, Nakao-Inoue H, Molofsky AV, Oldham MC. Variation among intact tissue
825 samples reveals the core transcriptional features of human CNS cell classes. *Nat Neurosci* **21**,
826 1171-1184 (2018).

827 20. Zeisel A*, et al.* Brain structure. Cell types in the mouse cortex and hippocampus revealed
828 by single-cell RNA-seq. *Science* **347**, 1138-1142 (2015).

829 21. Picelli S, Faridani OR, Björklund AK, Winberg G, Sagasser S, Sandberg R. Full-length
830 RNA-seq from single cells using Smart-seq2. *Nat Protoc* **9**, 171-181 (2014).

831 22. Matias I, Morgado J, Gomes FCA. Astrocyte heterogeneity: impact to brain aging and
832 disease. *Front Aging Neurosci* **11**, 59 (2019).

833 23. Sun W*, et al.* Glutamate-dependent neuroglial calcium signaling differs between young
834 and adult brain. *Science* **339**, 197-200 (2013).

835 24. Lein ES*, et al.* Genome-wide atlas of gene expression in the adult mouse brain. *Nature*
836 **445**, 168-176 (2007).

837 25. Batiuk MY*, et al.* An immunoaffinity-based method for isolating ultrapure adult
838 astrocytes based on ATP1B2 targeting by the ACSA-2 antibody. *J Biol Chem* **292**, 8874-
839 8891 (2017).

840 26. Satija R, Farrell JA, Gennert D, Schier AF, Regev A. Spatial reconstruction of single-cell
841 gene expression data. *Nat Biotechnol* **33**, 495-502 (2015).

842 27. Huang da W, Sherman BT, Lempicki RA. Systematic and integrative analysis of large
843 gene lists using DAVID bioinformatics resources. *Nat Protoc* **4**, 44-57 (2009).

844 28. Consortium TU. UniProt: the universal protein knowledgebase. *Nucleic Acids Res* **45**,
845 D158-D169 (2017).

846 29. Allen NJ, Lyons DA. Glia as architects of central nervous system formation and function.
847 *Science* **362**, 181-185 (2018).

848 30. Verkhratsky A, Nedergaard M. Physiology of astroglia. *Physiol Rev* **98**, 239-389 (2018).

849 31. Allen NJ, Eroglu C. Cell biology of astrocyte-synapse interactions. *Neuron* **96**, 697-708
850 (2017).

851 32. Zhang Y, Barres BA. Astrocyte heterogeneity: an underappreciated topic in neurobiology.
852 *Curr Opin Neurobiol* **20**, 588-594 (2010).

853 33. Pilz GA*, et al.* Live imaging of neurogenesis in the adult mouse hippocampus. *Science*
854 **359**, 658-662 (2018).

855 34. Chaker Z, Codega P, Doetsch F. A mosaic world: puzzles revealed by adult neural stem
856 cell heterogeneity. *Wiley Interdiscip Rev Dev Biol* **5**, 640-658 (2016).

857 35. Takata N, Hirase H. Cortical layer 1 and layer 2/3 astrocytes exhibit distinct calcium
858 dynamics *in vivo*. *PLoS One* **3**, e2525 (2008).

859 36. Grosche A*, et al.* Versatile and simple approach to determine astrocyte territories in
860 mouse neocortex and hippocampus. *PLoS One* **8**, e69143 (2013).

861 37. García-Marqués J, López-Mascaraque L. Clonal identity determines astrocyte cortical
862 heterogeneity. *Cereb Cortex* **23**, 1463-1472 (2013).

863 38. Paukert M, Agarwal A, Cha J, Doze VA, Kang JU, Bergles DE. Norepinephrine controls
864 astroglial responsiveness to local circuit activity. *Neuron* **82**, 1263-1270 (2014).

865 39. Yoshimura Y, Dantzker JL, Callaway EM. Excitatory cortical neurons form fine-scale
866 functional networks. *Nature* **433**, 868-873 (2005).

867 40. Lee I, Yoganarasimha D, Rao G, Knierim JJ. Comparison of population coherence of
868 place cells in hippocampal subfields CA1 and CA3. *Nature* **430**, 456-459 (2004).

869 41. Bayraktar OA*, et al.* Single-cell *in situ* transcriptomic map of astrocyte cortical layer
870 diversity. Preprint at https://doi.org/10.1101/432104 (2018).

871 42. Blanco-Suarez E, Liu TF, Kopelevich A, Allen NJ. Astrocyte-secreted Chordin-like 1
872 drives synapse maturation and limits plasticity by increasing synaptic GluA2 AMPA
873 receptors. *Neuron* **100**, 1116-1132 e1113 (2018).

874 43. Hochstim C, Deneen B, Lukaszewicz A, Zhou Q, Anderson DJ. Identification of
875 positionally distinct astrocyte subtypes whose identities are specified by a homeodomain
876 code. *Cell* **133**, 510-522 (2008).

877 44. Tsai HH*, et al.* Regional astrocyte allocation regulates CNS synaptogenesis and repair.
878 *Science* **337**, 358-362 (2012).

879 45. Supèr H, Soriano E, Uylings HB. The functions of the preplate in development and
880 evolution of the neocortex and hippocampus. *Brain Res Brain Res Rev* **27**, 40-64 (1998).

881 46. Ge WP, Miyawaki A, Gage FH, Jan YN, Jan LY. Local generation of glia is a major
882 astrocyte source in postnatal cortex. *Nature* **484**, 376-380 (2012).

883 47. Costa MR, Kessaris N, Richardson WD, Götz M, Hedin-Pereira C. The marginal
884 zone/layer I as a novel niche for neurogenesis and gliogenesis in developing cerebral cortex.
885 *J Neurosci* **27**, 11376-11388 (2007).

886 48. Rusnakova V, Honsa P, Dzamba D, Ståhlberg A, Kubista M, Anderova M. Heterogeneity
887 of astrocytes: from development to injury - single cell gene expression. *PLoS One* **8**, e69734
888 (2013).

889 49. Farmer WT*, et al.* Neurons diversify astrocytes in the adult brain through sonic hedgehog
890 signaling. *Science* **351**, 849-854 (2016).

891 50. Garcia AD, Petrova R, Eng L, Joyner AL. Sonic hedgehog regulates discrete populations
892 of astrocytes in the adult mouse forebrain. *J Neurosci* **30**, 13597-13608 (2010).

893 51. Clavreul S*, et al.* Cortical astrocytes develop in a plastic manner at both clonal and
894 cellular levels. *Nat Commun* **10**, 4884 (2019).

895 52. Farmer WT, Murai K. Resolving astrocyte heterogeneity in the CNS. *Front Cell Neurosci*
896 **11**, 300 (2017).

897 53. Morel L, Higashimori H, Tolman M, Yang Y. VGluT1+ neuronal glutamatergic signaling
898 regulates postnatal developmental maturation of cortical protoplasmic astroglia. *J Neurosci*
899 **34**, 10950-10962 (2014).

900 54. Papouin T, Henneberger C, Rusakov DA, Oliet SHR. Astroglial versus neuronal D-
901 serine: fact checking. *Trends Neurosci* **40**, 517-520 (2017).

902 55. Hochgerner H, Zeisel A, Lönnerberg P, Linnarsson S. Conserved properties of dentate
903 gyrus neurogenesis across postnatal development revealed by single-cell RNA sequencing.
904 *Nat Neurosci* **21**, 290-299 (2018).

905 56. Artegiani B, Lyubimova A, Muraro M, van Es JH, van Oudenaarden A, Clevers H. A
906 single-cell RNA sequencing study reveals cellular and molecular dynamics of the
907 hippocampal neurogenic niche. *Cell Rep* **21**, 3271-3284 (2017).

908 57. van den Brink SC*, et al.* Single-cell sequencing reveals dissociation-induced gene
909 expression in tissue subpopulations. *Nat Methods* **14**, 935-936 (2017).

910 58. Sakers K*, et al.* Astrocytes locally translate transcripts in their peripheral processes. *Proc*
911 *Natl Acad Sci U S A* **114**, E3830-E3838 (2017).

912 59. Fuzik J*, et al.* Integration of electrophysiological recordings with single-cell RNA-seq
913 data identifies neuronal subtypes. *Nat Biotechnol* **34**, 175-183 (2016).

914 60. Beckervordersandforth R*, et al. In vivo* fate mapping and expression analysis reveals
915 molecular hallmarks of prospectively isolated adult neural stem cells. *Cell Stem Cell* **7**, 744-
916 758 (2010).

917 61. Kharchenko PV, Silberstein L, Scadden DT. Bayesian approach to single-cell differential
918 expression analysis. *Nat Methods* **11**, 740-742 (2014).

62. Ting JT*, et al.* Preparation of acute brain slices using an optimized N-Methyl-D-glucamine protective recovery method. *J Vis Exp*, (2018).

63. Rasmussen R, Nedergaard M, Petersen NC. Sulforhodamine 101, a widely used astrocyte marker, can induce cortical seizure-like activity at concentrations commonly used. *Sci Rep* **6**, 30433 (2016).

64. Nimmerjahn A, Kirchhoff F, Kerr JN, Helmchen F. Sulforhodamine 101 as a specific marker of astroglia in the neocortex *in vivo*. *Nat Methods* **1**, 31-37 (2004).

## AUTHOR CONTRIBUTIONS

MGH conceived and directed the project. MYB developed the astrocyte isolation protocol, developed the modified Smart-seq2 protocol and prepared single cell cDNA libraries. MYB, FdV, CM, CK and JK performed ISH experiments. MYB performed gene function analysis on enriched genes using Uniprot and performed secondary analysis of the $Ca^{2+}$ imaging data. MYB and AM performed DAVID analysis. JW obtained the $Ca^{2+}$ imaging data and performed the primary analysis. AM performed bioinformatics analysis of sequencing data, under the guidance of TGB and CPP, as well as quantification of ISH data and development of the online database. JFV and JFO provided expert input on morphology analysis. TV provided access to equipment. MGH performed data analysis and wrote the final manuscript, with input from all co-workers, particularly MYB, AM and TGB. All authors approved submission.

## ACKNOWLEDGEMENTS

MGH grateful acknowledges support from the European Research Council (Starting Grant 281961), Fonds Wetenschappelijk Onderzoek (FWO) (Grants G066715N and 1523014N), Stichting Alzheimer Onderzoek (SAO) (S#16025), VIB Institutional Support and VIB Tech Watch funding. AM holds a SAO Pilot Grant (20180024). JW is a FWO Postdoctoral Fellow (12V7519N). TGB and CPP were supported by the Medical Research Council and received additional support from the European Union Seventh Framework Programme (FP7/2007-2013) under grant agreement no. 604102 (Human Brain Project). TV is supported by the FWO (G066715N and I001818N) and infrastructure grants (type 1 funding from the Hercules Foundation – AKUL/13/41 and Foundation Against Cancer project 2015-143).

The authors wish to acknowledge access to various core units at VIB-KU Leuven during this project. These include the KU Leuven FACS core, LIMONE imaging unit, VIB Nucleomics core and VIB Electrophysiology unit. Large capacity image storage was possible through ISPAMM funding (AKUL/13/39). We acknowledge Maroussia Hennes, Pieter De Bleser,

954 Mark Fiers, Ligia Mateiu, Pier Andrée Penttila and Keimpe Wierda for help at various stages
955 of this project. We also thank Drs. Pierre Vanderhaeghen, Dietmar Schmucker, Carlos
956 Fitzsimons, Omer Bayraktar and David Rowitch for discussion, critical comments and
957 advice.

958

959 **COMPETING INTERESTS:** TGB is currently chief executive officer at The
960 Bioinformatics CRO. The remaining authors declare no competing interests.

961

962

**FIGURE LEGENDS.**

**Figure 1: Single cell sequencing strategy and cell type identification.** (a) Whole brains were obtained from C57Bl/6J mice at post-natal (P) day 56. Cortical (CX) and hippocampal (HP) astrocytes were prepared separately, using enzymatic digestion followed by mechanical trituration. Two separate batches of astrocytes for each region were prepared. Cortical cell suspensions were prepared from two littermate animals in parallel using separate tubes. Hippocampal cell suspensions were also prepared in parallel using separate tubes; in this case two different sets of four littermate animals were used. Astrocytes were then specifically labeled with the ASCA-2-PE antibody and single cells were deposited in individual wells of a PCR plate using FACS. Single cell library preparation was performed using a modified Smart-seq2 protocol. In total, 2,976 libraries were prepared and sequenced using a NextSeq 500 system (Illumina). (b) Each library was sequenced to optimal coverage (on average 1M reads per library). 2,015 high quality libraries were retained for further analysis. In these libraries, a high fraction of reads mapped to exons (CDS, coding sequence; UTR, untranslated region). Conversely, a low fraction of reads mapped to intronic and intergenic regions. (c) Visualization of the major higher order cell types (2,015 cells) identified by Seurat using tSNE plots. Each dot represents a single cell. Cells with similar molecular profiles group together; cell types were assigned according to the expression of specific marker genes (and are labeled in different colors). (d) Gene expression heatmap for higher order cell types (columns) grouped according to the Seurat classification shown in Figure 1c. Color-coding from Figure 1c is retained. Grey, no expression; yellow, low expression; red, high expression. Ln-normalized gene expression data is shown.

**Figure 2. Identification of astrocyte subtypes in adult mouse cortex and hippocampus.** **S**ingle cell data was used to identify distinct astrocyte subtypes (AST). (a) 1,811 astrocytes were identified from higher order clustering. This data was extracted and reclustered using Seurat and 5 distinct astrocyte subtypes were identified. Clusters are presented in tSNE plots, with each AST color-coded. (b) Hierarchically clustered average gene expression heatmap for genes overexpressed across subtypes. Rows correspond to cells, columns to genes. Magenta, low gene expression; yellow, high expression. Scaled ln-normalized data is shown. (c) Astrocytes derived from cortex (CX) or hippocampus (HP) segregate based on gene expression. (d) Expression of subtype-specific marker genes selected for *in situ* hybridization experiments. Markers are classed as absent/low '-' or highly expressed '+', based on ln-normalized expression data. See also Supplementary File 2.

**Figure 3. Identification of common and differentially expressed genes in astrocytes.** (a) Chart showing the number of genes expressed in at least 60% of sampled astrocytes (common) and the number of genes specifically enriched in each subtype. (b) Examples of

genes common across astrocyte subtypes, classified by biological function. TFs, transcription factors. (c) Examples of genes highly enriched in specific astrocyte subtypes, classified by biological function. Note, some genes, for example *Gabrg1* (gamma-aminobutyric acid type A receptor gamma 1 subunit), could be classified as either an ion channel or as involved in synaptic function/plasticity. Here, classification was based on the principal identified function – ion channel activity.

**Figure 4. Differential patterning of AST4 and AST5 in adult mouse brain**. Multiplexed fluorescence *in situ* hybridization was used to map locations of AST4 and AST5. (a) AST4 was identified by high expression levels of *Frzb, Ascl1* and *Slc1a3*. (b) AST5 was identified by absence/low expression of *Ogt* and high expression of both *Fam107a* and *Slc1a3*. Mapping was performed on three sections obtained from three independent animals aged between P56-P60. Representative images are shown. Top left: low magnification image of a coronal section. Black dots show the distribution of the astrocyte subtype through one brain hemisphere. Brain regions are defined manually based on definitions from the Allen Brain Atlas. High magnification images (below) show the localization of markers to specific cells defined on the basis of nuclear (DAPI, blue) staining. Right: bar plots (showing from left to right) fluorescence counts per RNA marker per cell (shown for all cells across all sections analyzed), the distribution of the subtype between brain regions and the distribution of the subtype normalized to the total number of astrocytes per brain region (all *Slc1a3*+ cells). Astrocytes belonging to the subtype of interest are highlighted by a shaded box (color-coded according to the scheme used in Figure 2a). Astrocyte numbers across layers are given as average per section analyzed. Error bars are equivalent across the figure and represent SEM. Scale bars, low magnification 1000 μm; high magnification, 10 μm. '+' high gene expression, '-' low or absent gene expression. SO, Stratum oriens: SP, Stratum pyramidale: SR, Stratum radiatum: SG, Subgranular zone: \DG, Dentate gyrus without SG: SLM, Stratum lacunosum-moleculare.

**Figure 5. Differential patterning of AST1 and AST2 in adult mouse brain**. Multiplexed fluorescence *in situ* hybridization was used to map locations of AST1 and AST2. (a) AST1 was identified by high expression levels of *Gfap, Agt* and *Slc1a3*. (b) AST2 was identified by low expression/absence of *Agt* and high expression of both *Unc13c* and *Slc1a3.* Mapping was performed on three sections obtained from three independent animals aged between P56-P60. Representative images are shown. Top left: low magnification image of a coronal section. Black dots show the distribution of the astrocyte subtype through one brain hemisphere. Brain regions are defined manually based on definitions from the Allen Brain Atlas. High magnification images (below) show the localization of markers to specific cells defined on the basis of nuclear (DAPI, blue) staining. Right: bar plots (showing from left to right)

fluorescence counts per RNA marker per cell (shown for all cells across all sections analyzed), the distribution of the subtype between brain regions and the distribution of the subtype normalized to the total number of astrocytes per brain region (all *Slc1a3*+ cells). Astrocytes belonging to the subtype of interest are highlighted by a shaded box (color-coded according to the scheme used in Figure 2a). Astrocyte numbers across layers are given as average per section analyzed. Error bars are equivalent across the figure and represent SEM. Scale bars, low magnification 1000 μm; high magnification, 10 μm. '+' high gene expression, '-' low or absent gene expression. SO, Stratum oriens: SP, Stratum pyramidale: SR, Stratum radiatum: SG, Subgranular zone: \DG, Dentate gyrus without SG: SLM, Stratum lacunosum-moleculare.

**Figure 6. Differential patterning of AST3 in adult mouse brain.** Multiplexed fluorescence *in situ* hybridization was used to map the location of AST3. Due to technical limitations, AST3 was mapped using a split marker approach. Sections were assessed for (a) low expression/absence of *Gfap* with expression of *Agt* and *Slc1a3* (to differentiate AST3 from AST1) and (b) low expression/absence of *Unc13c* with expression of *Agt* and *Slc1a3* (to discriminate between AST3 and AST2). Mapping was on three sections from three independent animals aged P56-P60. Representative images are shown. Top left: low magnification image of a coronal section. Black dots show astrocyte subtype distribution through one hemisphere. Regions are defined manually based on the Allen Brain Atlas. High magnification images (below) show the localization of markers to specific cells based on nuclear (DAPI, blue) staining. Right: bar plots (showing left to right) fluorescence counts per marker per cell (for all cells across all sections analyzed), the distribution of the subtype between brain regions and the distribution of the subtype normalized to the number of astrocytes per brain region (all *Slc1a3*+ cells). Astrocytes belonging to the subtype of interest are highlighted by a shaded box (color-coded according to the scheme used in Figure 2a). Astrocyte numbers across layers are given as average per section analyzed. Error bars are equivalent across the figure and represent SEM. Scale bars, low magnification 1000 μm; high magnification, 10 μm. '+' high gene expression, '-' low or absent gene expression. SO, Stratum oriens: SP, Stratum pyramidale: SR, Stratum radiatum: SG, Subgranular zone: \DG, Dentate gyrus without SG: SLM, Stratum lacunosum-moleculare.

**Figure 7. Schematic summary of astrocyte subtype positions in adult mouse brain.** Indicated positions are based on *in situ* hybridization data (Figures 4-6) and are marked on a representative sagittal section of adult mouse brain (adapted from the Allen Mouse Brain Atlas). Subtypes are color-coded (as in Figure 2a). Scale bar, 500 μm.

**Figure 8. Astrocyte subpopulations display distinct $Ca^{2+}$ transient properties.** Calcium transients in SR101-labeled astrocytes were detected using Fluo-4. Measurements were made in acute brain slices containing cortical layer 1 (L1), cortical layers 3-5 (L3-5) and the CA1 region of the hippocampus (CA1). Transients were recorded under sequential conditions of baseline activity (BASE), tetrodotoxin (TTX) and TTX plus phenylephrine (PHE). (a) Representative astrocytes (arrowheads) and the calcium transients recorded from them under each experimental condition. Scale bar, 50 μm. (b) The total population of active astrocytes was defined as cells responding to application of PHE. The fraction of this population displaying $Ca^{2+}$ transients under BASE and TTX conditions is shown in blue. (c) Transient parameters grouped by brain region recorded. Numerical values are the means for each condition. (d) Hierarchical clustering of $Ca^{2+}$ transient parameters after application of PHE. (e) Proportion of astrocytes from the various brain regions per cluster defined in (d). (f) Astrocyte peak parameters grouped per cluster. One dot equals one cell in (c), (d) and (f). Plots in (c) and (f) show mean ± S.D. Data normality was tested using a Shapiro-Wilk test. Significant differences were verified using a Kruskal-Wallis test with *post-hoc* Dunn's test, with *p*-values adjusted with the Benjamini-Hochberg method. *$p \leq 0.05$, **$p \leq 0.01$, ***$p \leq 0.001$. AUC – area under the curve. Nine animals were used. In total 614 cells were analyzed.

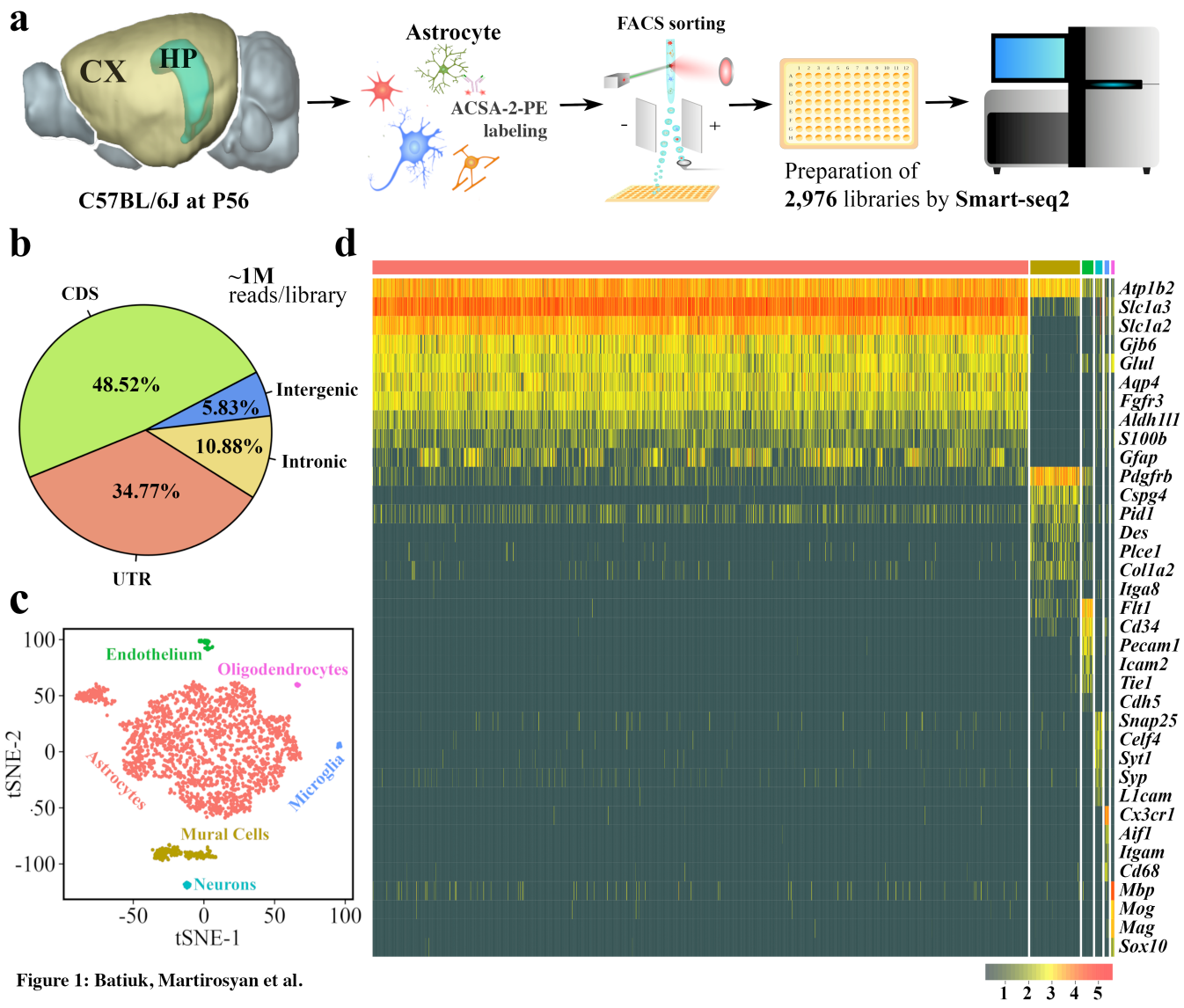


**Figure 1: Batiuk, Martirosyan et al.**

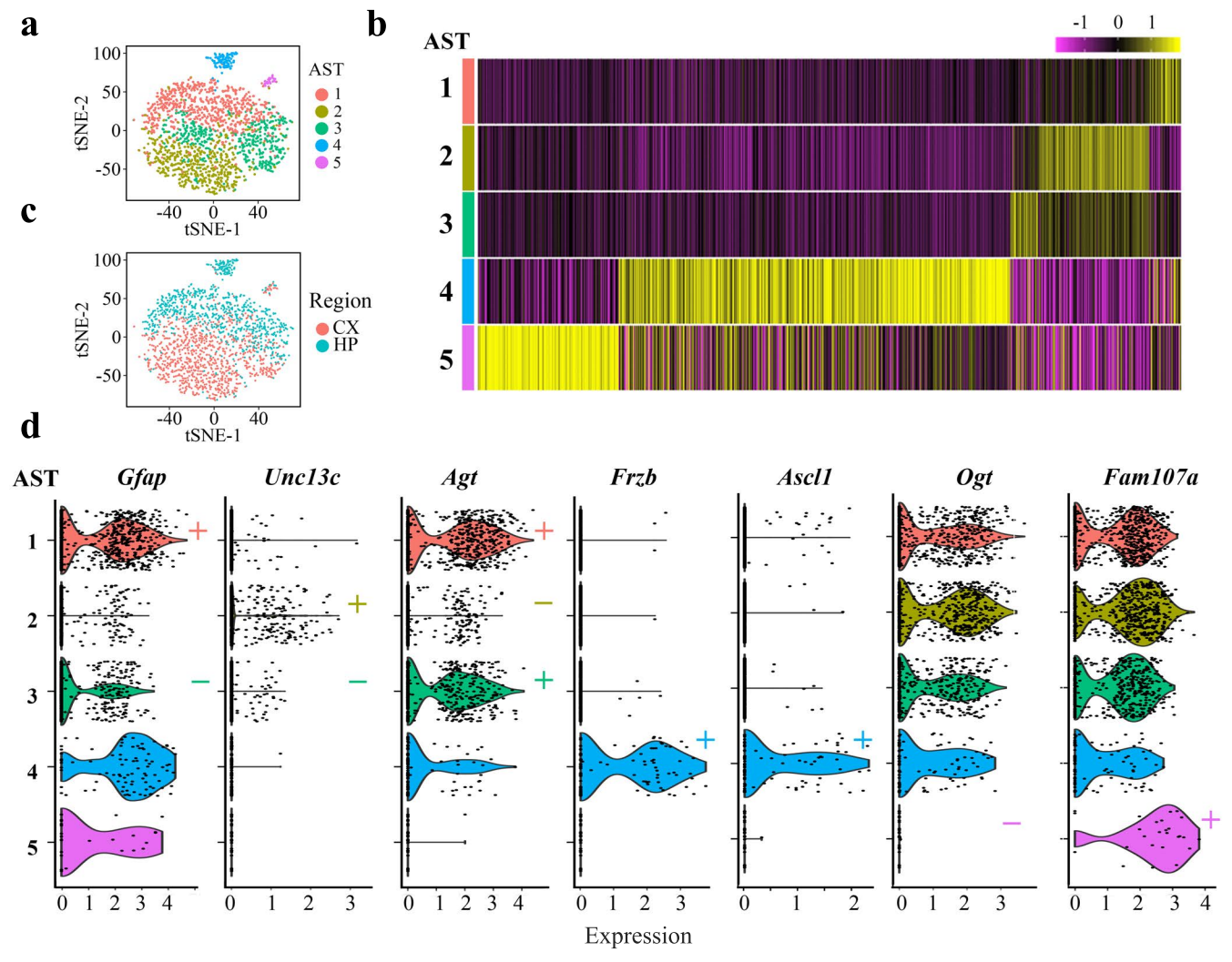


**Figure 2: Batiuk, Martirosyan et al.**

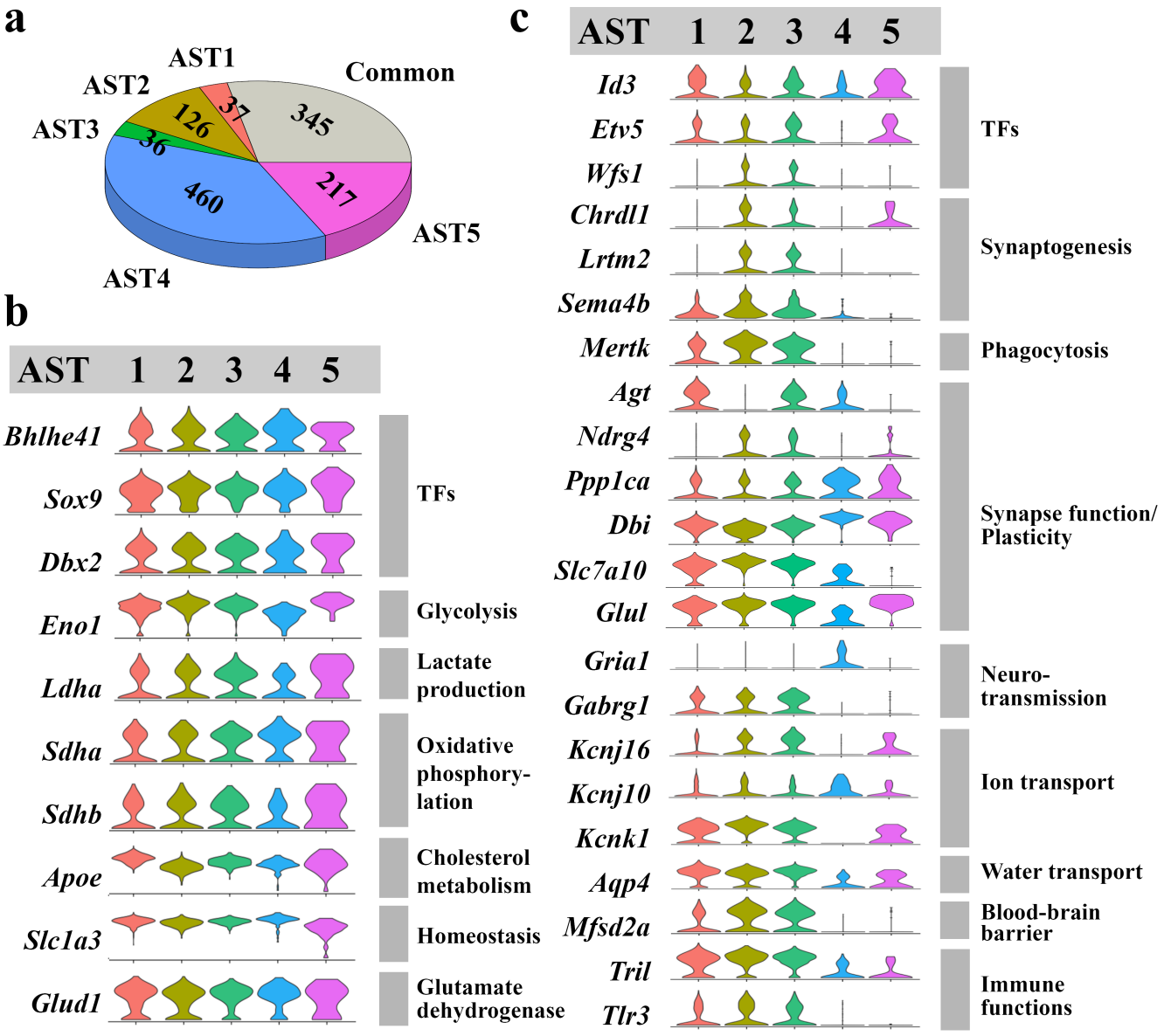


Figure 3: Batiuk, Martirosyan et al.

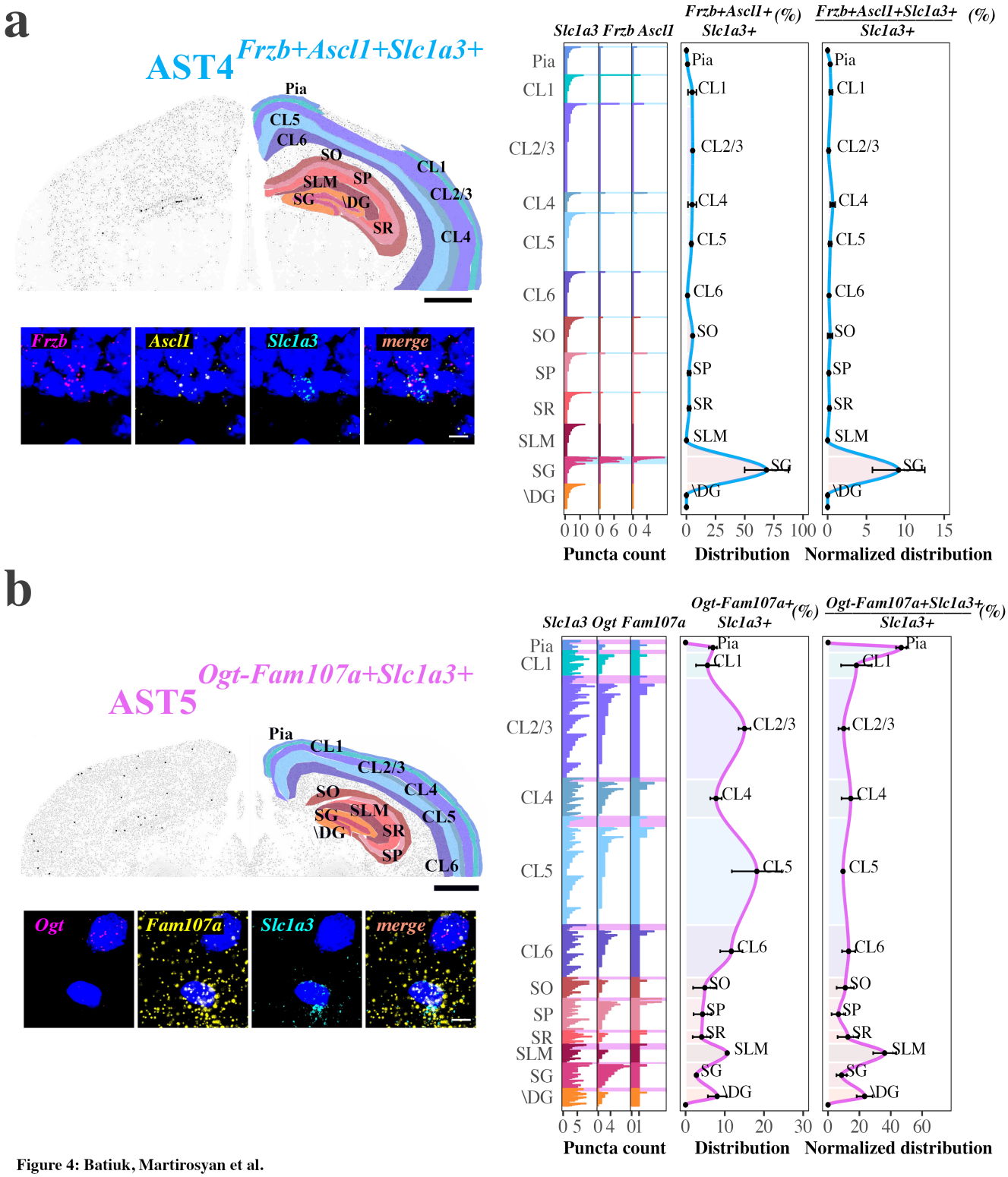


**Figure 4: Batiuk, Martirosyan et al.**

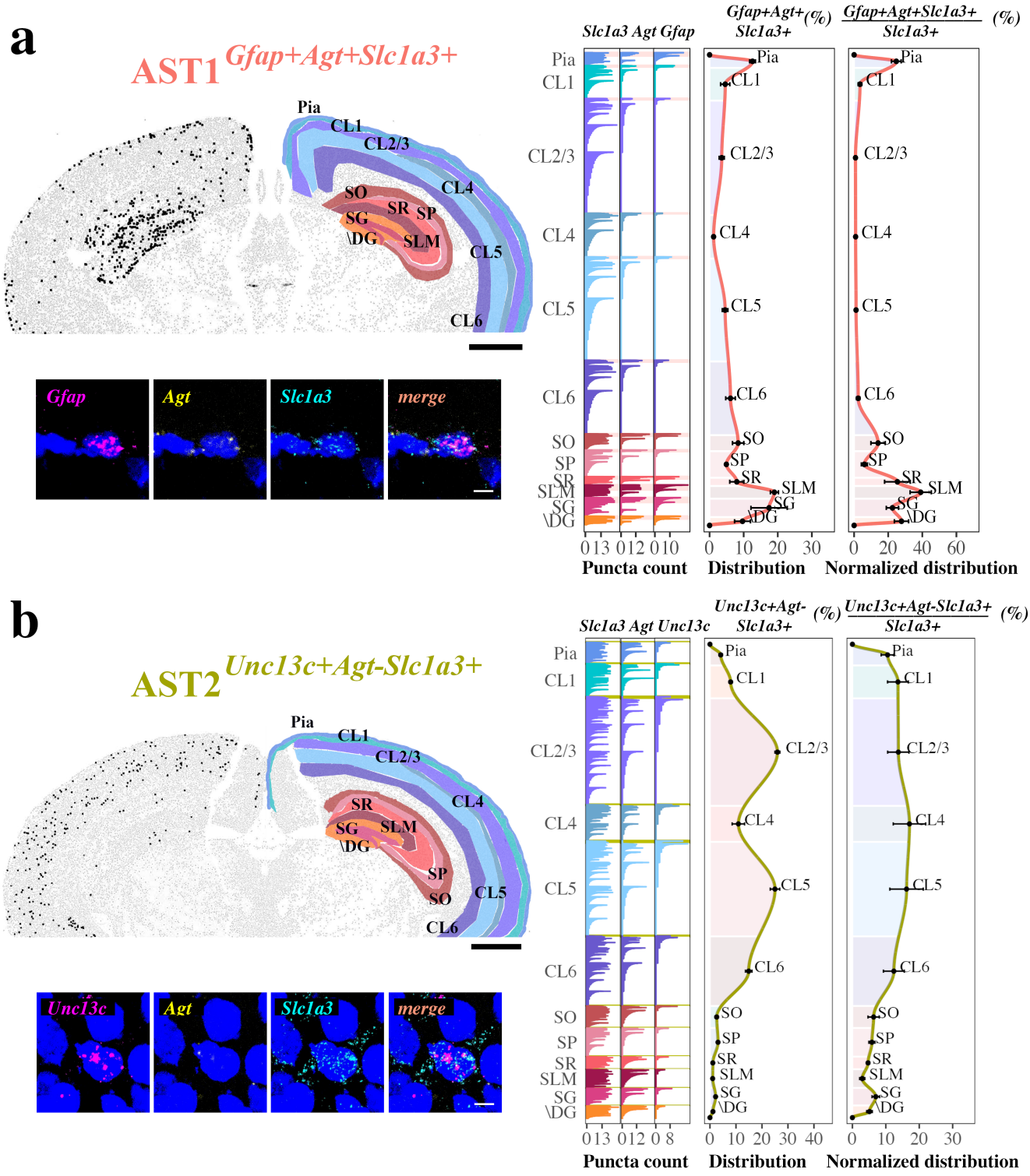


**Figure 5: Batiuk, Martirosyan et al.**

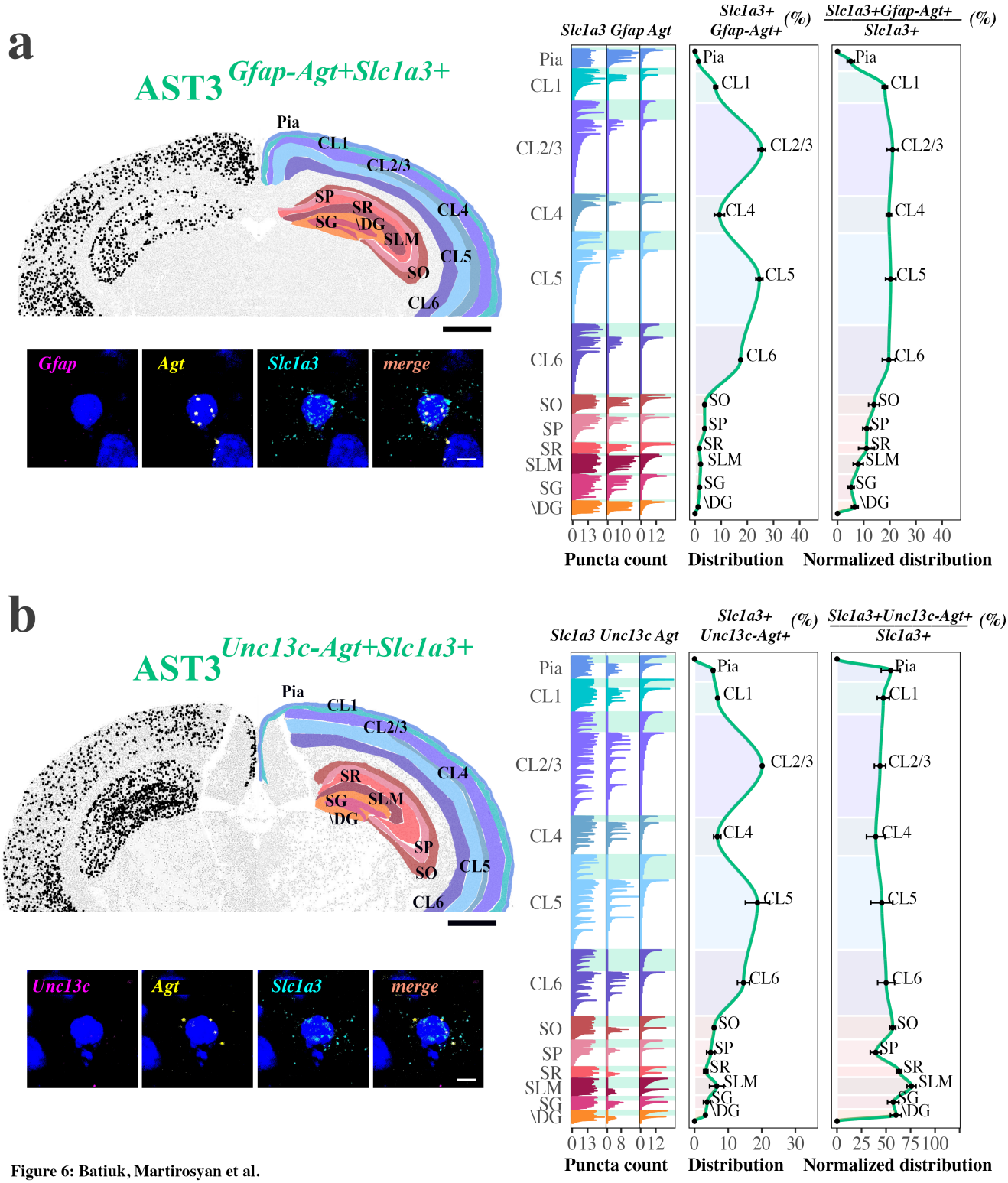


Figure 6: Batiuk, Martirosyan et al.

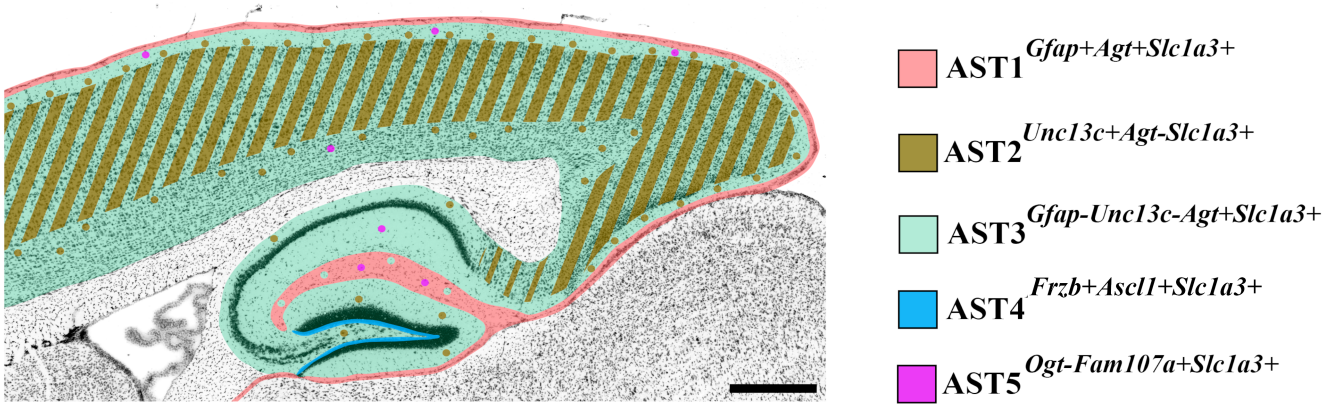


**Figure 7: Batiuk, Martirosyan et al.**

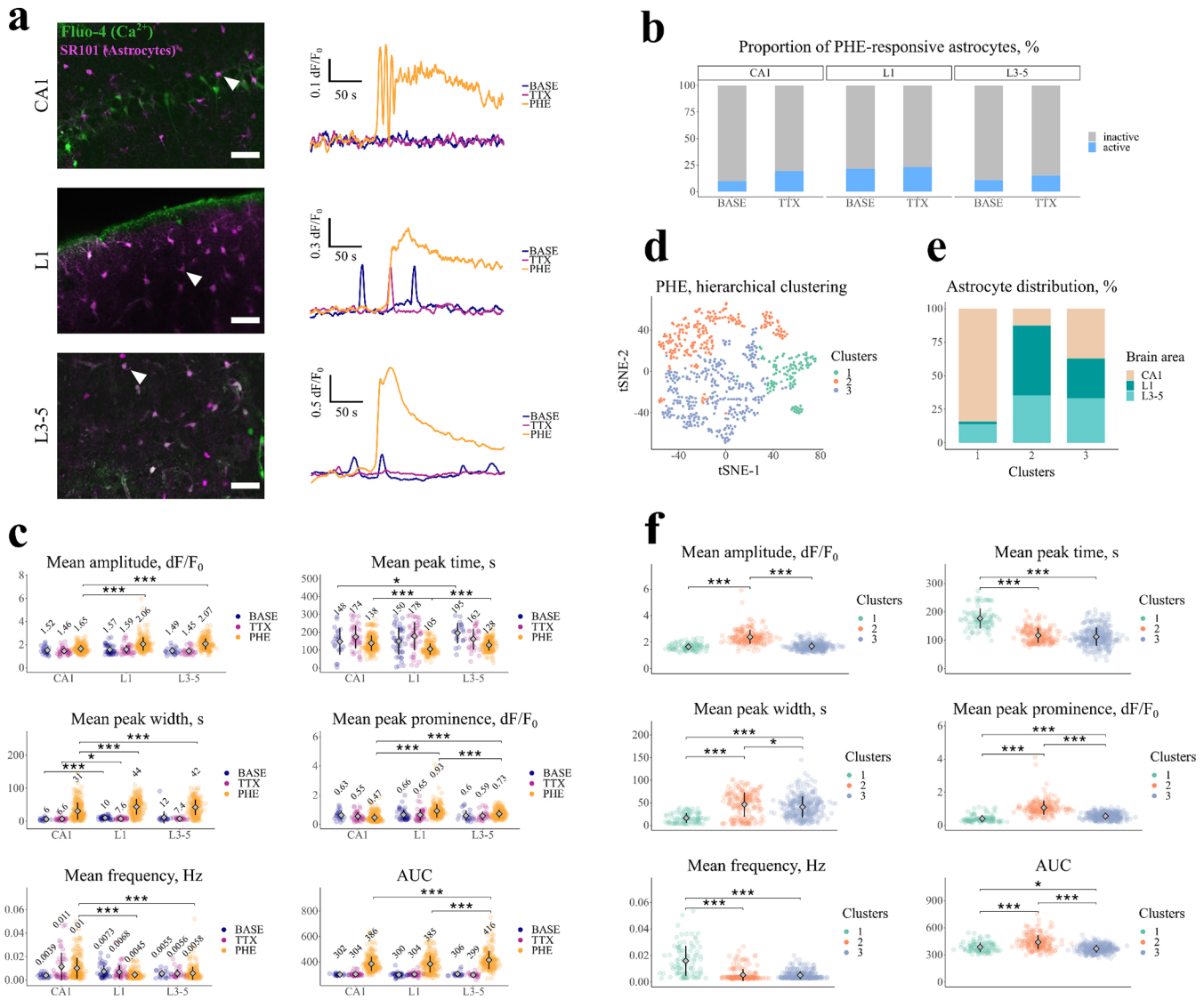


Batiuk, Martirosyan et al., Figure 8